

YY Hya and its interstellar environment

Stefan Kimeswenger^{1,2}, John R. Thorstensen³, Robert A. Fesen³, Marcel Drechsler⁴, Xavier Strottner⁵, Maicon Germiniani⁶, Thomas Steindl¹, Norbert Przybilla¹, Kathryn E. Weil⁷, and Justin Rupert⁸

¹ Institut für Astro- und Teilchenphysik, Leopold-Franzens Universität Innsbruck, Technikerstr. 25, 6020 Innsbruck, Austria
e-mail: Stefan.Kimeswenger@uibk.ac.at

² Instituto de Astronomía, Universidad Católica del Norte, Av. Angamos 0610, Antofagasta, Chile

³ Department of Physics and Astronomy, 6127 Wilder Laboratory, Dartmouth College, Hanover, NH 03755-3528, USA

⁴ Sternwarte Bärenstein, Feldstraße 17, 09471 Bärenstein, Germany

⁵ Montfrazze, 01370 Saint Etienne Du Bois France

⁶ Leopoldo Stadtlober Street 49, 89871-000 Serra Alta, Brazil

⁷ Department of Physics and Astronomy, Purdue University, 525 Northwestern Avenue, West Lafayette, IN 47907 USA

⁸ MDM Observatory, Kitt Peak National Observatory, 950 N. Cherry Ave., Tucson, AZ 85719, USA

Accepted: October 8th, 2021

ABSTRACT

Context. During a search for previously unknown Galactic emission nebulae, we discovered a faint 36' diameter H α emission nebula centered around the periodic variable YY Hya. Although this star has been classified as RR-Lyr variable, such a stellar classification is inconsistent with the formation of such a large nebula especially if at YY Hya's estimated Gaia distance of ≈ 450 pc. GALEX image data also shows YY Hya to have a strong UV excess, suggesting the existence of a hot, compact binary companion.

Aims. We aim to clarify the nature of YY Hya and its nebula.

Methods. In addition to our discovery image data, we obtained a 2.5×2.5 image mosaic of the whole region with CHILESCOPE facilities and time-series spectroscopy at MDM observatory. Also, we used data from various space missions to derive an exact orbital period and a spectral energy distribution (SED). The binary star model code Binary Maker 3 (BM3), and Kurucz ATLAS9 stellar atmospheres were used to derive a synthetic light curve and a model SED of the compact binary system, respectively.

Results. We find that YY Hya is a compact binary system containing a K dwarf star which is strongly irradiated by a hot white dwarf (WD) companion. The spectral characteristics of the emission lines, visible only during maximum light of the perfectly sinusoidal optical light curve, when the side of the K star fully illuminated by the WD points to the observer, shows signatures much like members of the BE UMa variable family. These are post common envelope pre-cataclysmic variables. However the companion star here is more massive than found in other group members and the progenitor of the white dwarf must have been a 3 to 4 M_{\odot} star. The nebula seems to be an ejected common envelope shell with a mass in the order of one M_{\odot} and an age of 500 000 years. This makes it to be the biggest hitherto known such shell. Alignment of neighboring nebulosities some 45' to the northeast and southwest of YY Hya suggests that the system had strong bipolar outflows. We briefly speculate it might be related to the 1065 BP "guest-star" reported in ancient Chinese records as well.

Key words. Stars: novae, cataclysmic variables — Stars: white dwarfs — ISM: evolution — Stars: individual: YY Hya — Stars: binaries: symbiotic — circumstellar matter

1. Introduction

In a systematic search for previously unrecognized Galactic nebulosities on sky survey plates downloaded from the SuperCOSMOS facility archive in Edinburgh¹ (Hambly et al. 2001), we discovered a small bow-like emission structure near $\alpha(J2000) = 09:25:50$, $\delta(J2000) = -22:23:00$. Follow-up images taken with a small telescope facility at Serra Alta, Brazil showed that this feature is the brightest part of a much larger (36'diameter), highly structured and nearly circular H α nebula centered on the variable star YY Hya ($\alpha = 09:26:20.596$, $\delta = -22:23:38.38$; $l = 252^{\circ}81$, $b = +19^{\circ}94$). We also found two additional emission structures, located $\sim 45'$ northeast and southwest of the center (see Fig. 1). First thought to be a possible planetary nebula (PN), it was assigned the identifier StDr Object 20 (PN G252.8+19.9) in the HASH PN data base (Parker et al. 2016, 2017).

YY Hya was discovered nearly 85 years ago as Harvard Variable No. 7525 (Boyce 1936) and classified as an RR Lyr star, called *Cluster* variable in the literature at that time. Guthnick & Prager (1936) assigned the name YY Hya shortly after that. Drake et al. (2017), using data from the Catalina Real-time Transient Survey (CRTS, Drake et al. 2009), determined a period of 0.33479 d, and classified the star as a c-type RR Lyr (RRc), based on its almost perfectly sinusoidal light curve and high amplitude of nearly one magnitude. The RRc classification implies an absolute magnitude range from $0^m85 < M_V < 0^m55$ (Catelan et al. 2004; Dambis et al. 2013). This led to an initial distance estimate of $4.05 < D_{RR} < 4.75$ kpc.

However, recent parallax measurements indicate a much shorter distance, inconsistent with any kind of RR Lyr star. The inverse of the parallax from Data Release 2 (DR2) of the Global Astrometric Interferometer for Astrophysics (Gaia; Gaia Collaboration et al. 2018) is 443 ± 6 pc, about 10 times smaller than that expected for an RR Lyr star. The more recent Gaia early Data Release 3 (eDR3; ?) gives 456 ± 3 pc. Although this new

¹ <http://www-wfau.roe.ac.uk/sss/pixel.html>

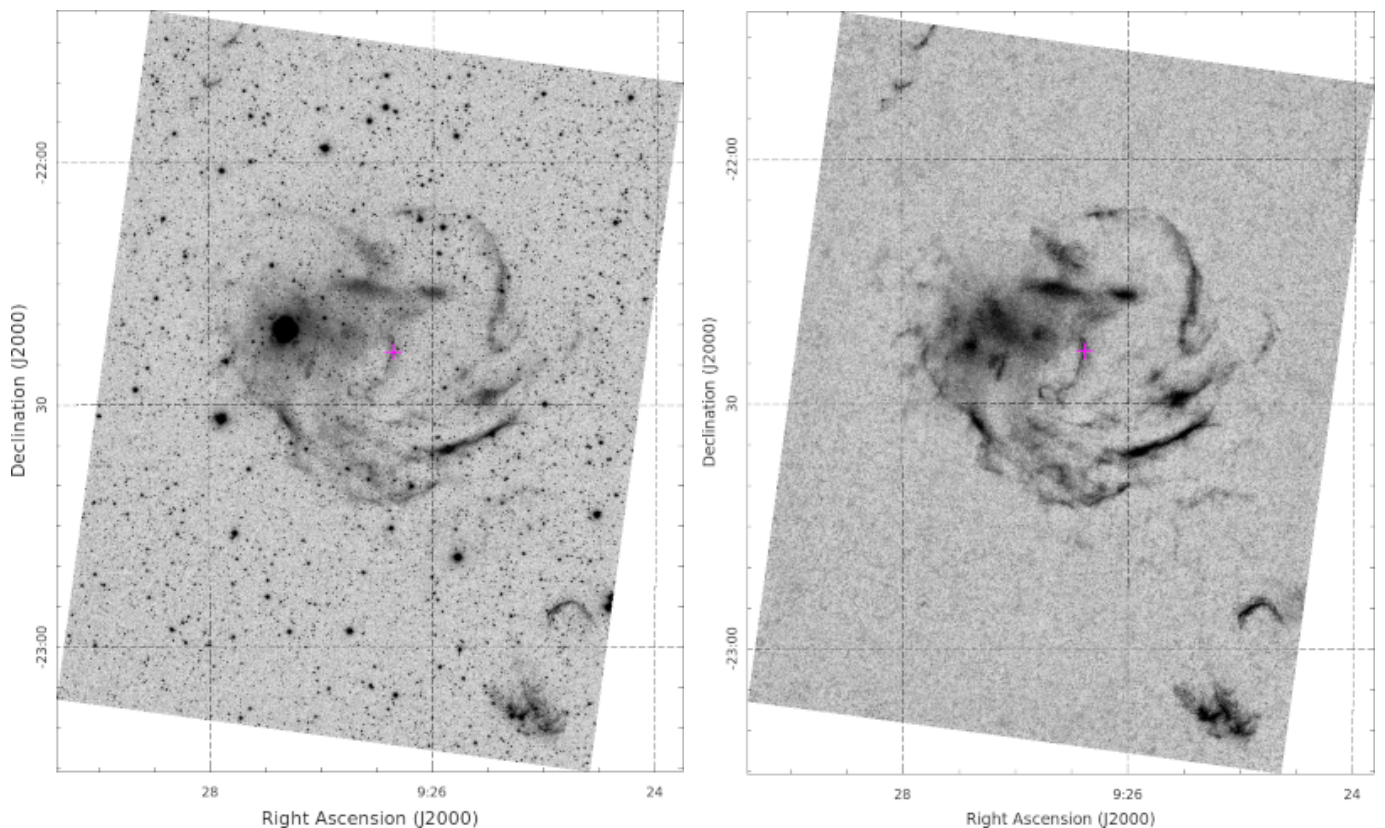


Fig. 1. The $H\alpha$ image taken at Serra Alta, Brazil of the region around YY Hya. (Left:) The original image; (right) the image after star removal procedure (see text). The inner main nebula has a diameter of $36''$. Clearly visible are in the northeast and in the southwest corner exactly vis-à-vis emission structures both $47''$ from the variable star. The northeast structure is just at the image edge and partly cut off.

value does not overlap within the 1σ errors with the DR2 result, we will adopt that value as it is based on more extensive data and has correspondingly smaller uncertainties. However, up to now, the Gaia analysis solves only for the star’s position, parallax, and proper motions. Moving due to binary orbits is not yet included in Gaia as a source of possible systematic errors. But in the case of the system here as we see later, the whole orbit extends only to 0.03 mas. That is about 1σ of the given parallax error in Gaia eDR3. The distance by Gaia thus seems to be still reliable. However the orbital motion might be the cause for the significant shift between the two major data releases. Thus the realistic error, assuming some systematic component, is more likely in the order of 10 pc.

In this paper, we present follow-up imaging and time series spectroscopy, along with photometric data collected from various literature and data base resources, as well as an analysis of photometry from the Transiting Exoplanet Survey Satellite (TESS, [Ricker et al. 2015](#)). We have used these data to classify the system using radial velocities, spectral energy distribution (SED) and the UV excess found by the Galaxy Evolution Explorer (GALEX, [Bianchi 1999](#)). We furthermore put the kinematic behavior of the system into the Galactic context and derive detailed parameters for the progenitor stars. Finally, we discuss a possible link to a medieval “guest-star” observation reported by Chinese observers in this direction on the sky ([Hsi 1957](#); [Ho 1962](#)).

2. Data and Reductions

2.1. $H\alpha$ Imaging

$H\alpha$ discovery images were taken in January 2020 in Serra Alta, Brazil², using a 115mm F7 TS Proline Triple APO refractor from Teleskop-Service Ransburg³ plus a focal reducer resulting in a final $f/5.5$. The detector was a ZWO⁴ Camera ASI 1600 MM-Cool equipped with a 4656×3520 , $3.8\mu\text{m}$ pixel CMOS Panasonic MN34230 and an OPTOLONG⁵ 7 nm wide $H\alpha$ filter. This resulted in a pixel scale of $1''.24 \text{ pixel}^{-1}$ and a field of view (FOV) of $1^\circ 6' \times 1^\circ 21'$.

The image shown in Fig. 1 is a composite of 120×600 s exposures for a total exposure time of 20 hours. A set of matching broadband red filter images were also obtained in order to remove the stellar background. These red filter images were stretched manually by a nonlinear intensity curve to correct for differences in the calibration and were finally subtracted from the $H\alpha$ image.

The resulting images shows a highly structured $H\alpha$ nebula with a diameter of $\sim 36''$. In addition, two smaller nebulosities in opposite directions roughly $45''$ to the northeast and southwest from YY Hya are also visible. Examination of copies of the original photographic sky surveys ESO-R ([West 1974](#)) shows no more evidence for the nebula other than the small southwestern arc already seen on the H-compressed digital scans. Likewise, no part of the nebula is visible at the SERC-J ([Morgan 1995](#))

² Serra Alta, Brazil: $53^\circ 04' 26''$ W, $26^\circ 7' 28''$ S

³ <https://www.teleskop-express.de/>

⁴ <https://astronomy-imaging-camera.com/>

⁵ <https://www.optolong.com/>

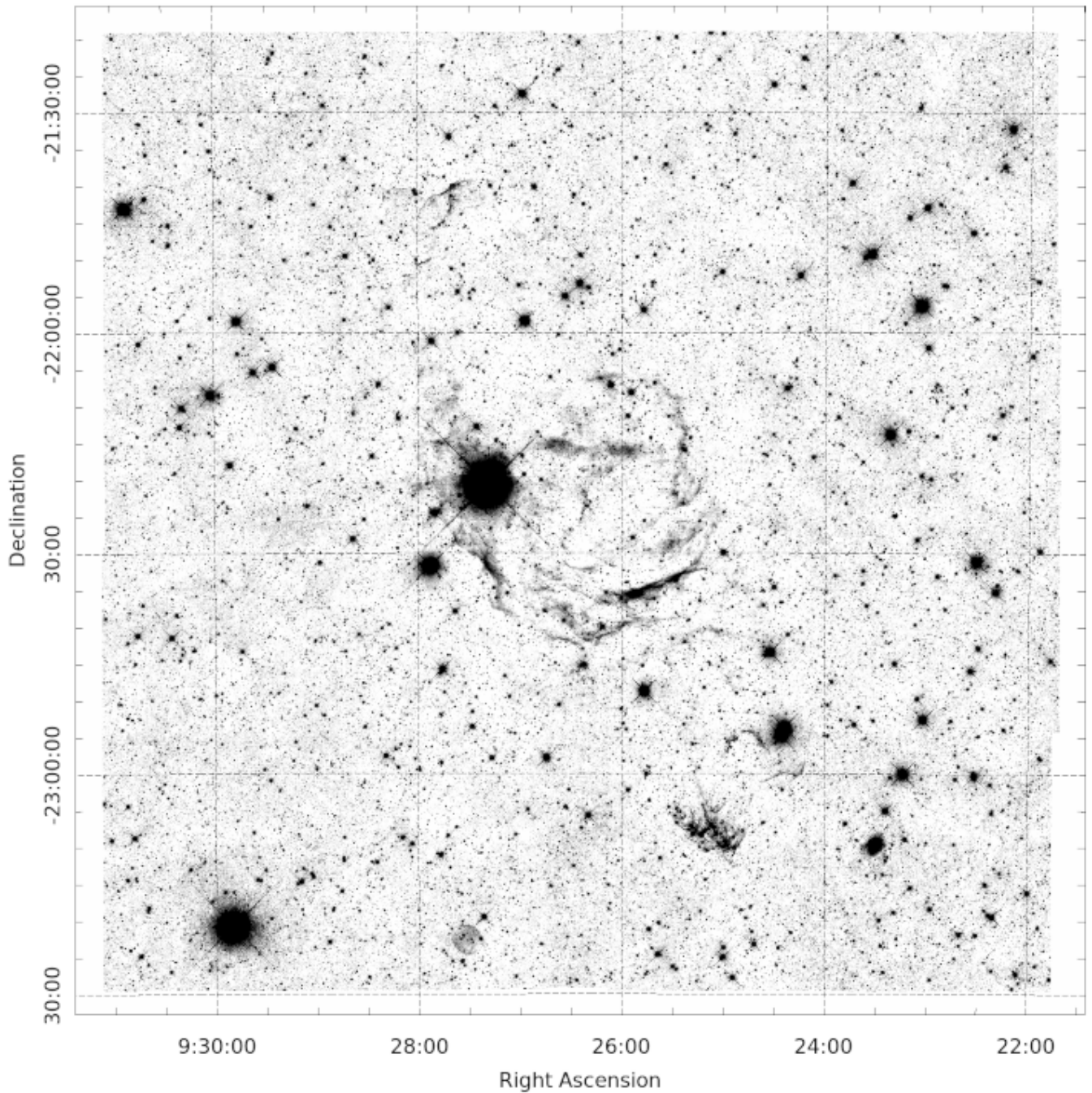


Fig. 2. The $H\alpha$ image mosaic obtained at CHILESCOPE with a linear gray-scale mapping with surface brightness from zero to $1.5 \cdot 10^{-16} \text{ erg cm}^{-2} \text{ s}^{-1} \text{ arcsec}^{-1}$. The stellar limiting magnitude is about Gaia RP $\approx 21^m 8$. The round nebula southwards is not related to our target but the beforehand known planetary nebula StDr 47 (PN G253.7+19.4, $09^h 27^m 31^s 46$, $-23^\circ 22' 34'' 40$).

plate copy, suggesting that the nebula does not have a significant [O III] emission.

To investigate further, we booked time at the CHILESCOPE remotely controlled commercial observatory facilities. Details on the location, the instrumentation used and the calibration are given in Appendix B. Images with $H\alpha$, [O III], and [S II] filters from Astrodon⁶ were obtained. However, 30 minutes of exposure in the [O III] and [S II] bands centered at the main nebula showed no detection of even the brightest filaments. Thus the campaign, lasting from March 9th to June 13th 2021, focused finally completely on the $H\alpha$ imaging. The aim was the full cover-

age of the field and the possible detection of further distant structures and a calibrated intensity estimate. But beside the already mentioned structures, no other distant structures related YY Hya and its nebula could be identified. Figure 2 shows the mosaic of the 294 $H\alpha$ images with 1200 seconds exposure time each (98 hours integration time). The brightest nebular filaments are about $4 \cdot 10^{-17} \text{ erg cm}^{-2} \text{ s}^{-1} \text{ arcsec}^{-2}$. The faintest visible structures at 1.5σ to the background *rms* of single pixels are around $8 \cdot 10^{-18} \text{ erg cm}^{-2} \text{ s}^{-1} \text{ arcsec}^{-2}$.

Higher-resolution images were also obtained with the 2.4m Hiltner telescope at the MDM Observatory at Kitt Peak, Arizona using the Ohio State Multi-Object Spectrograph (OSMOS;

⁶ <https://astrodon.com/>

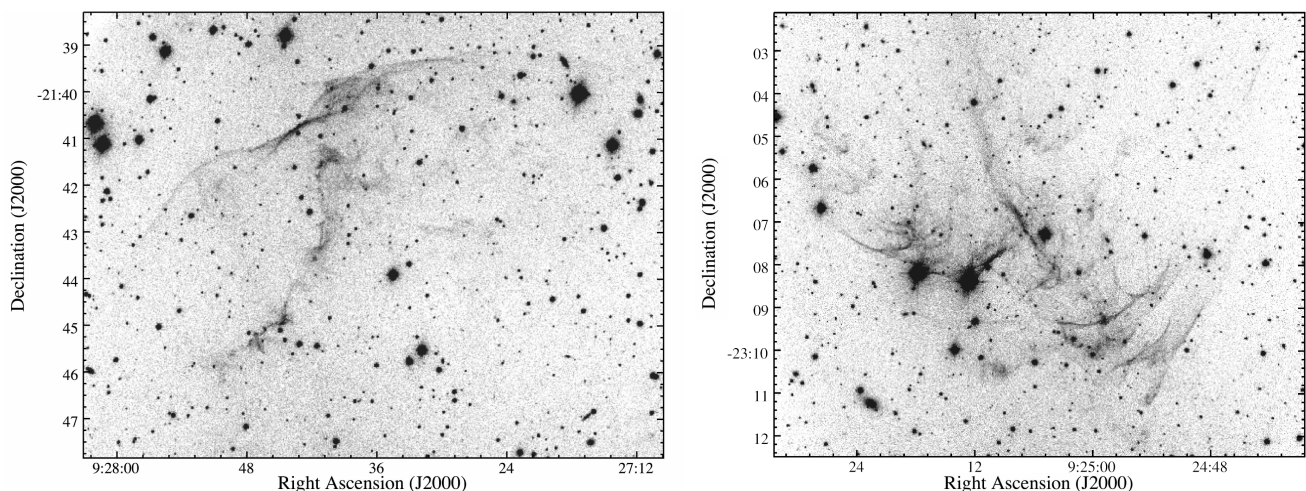


Fig. 3. MDM $H\alpha$ images of the northeastern (left) and southwestern (right) outlying nebulosities around YY Hya showing the presence of emissions of overlapping shocks.

Martini et al. 2011) in direct imaging mode. A $4k \times 4k$ CCD provided an effective FOV of $18' \times 18'$. With 2×2 on-chip binning, this yielded an image scale of $0.546'' \text{ pixel}^{-1}$. A series of narrow passband $H\alpha$ + [N II], [O III] $\lambda 5007$, and [S II] filter images were taken of the northeastern and southwestern outlying nebulosities with exposure times of 600 s to 1200 s. The resulting $H\alpha$ images of the NE and SW outlying nebulae are shown in Fig. 3. The sharp filamentary appearance of the emission along with the lack of appreciable [O III] and [S II] emissions strongly suggests these filaments are Balmer-dominated shock filaments with shock velocities $\approx 100 \text{ km s}^{-1}$ or more depending on the density of the ambient interstellar medium.

2.2. UV Images

UV GALEX images (Bianchi 1999; Martin et al. 2005) were obtained from the online data bases. This nearly all-sky UV imaging survey used wide-band filters centered around 154.9 and 230.5 nm, called FUV and NUV, respectively. The full-resolution images contain mainly pixels with individual photons in about 30% of the pixels and more than 60% of the image pixels containing no photons at all. Simply averaging these images would have artificially enhanced the intensity in the overlap regions of the individual pointings, while using a smoothing filter degrades the brighter parts of the image. We therefore used a nearest-neighbor algorithm in the way normally used for investigations of stellar cluster density (Gao 2016), which preserved the faint background without touching the brighter regions. Seven survey fields were combined that way to get a larger mosaic for the final image (Fig. 4).

Interestingly, only the far NE and SW pair of nebulae $\sim 45'$ from the center are clearly detected in the GALEX images. The average position angle of these features is 25° (north over east) on the sky. This is consistent with these outer emissions as being due to shocks, as suggested by the optical images. A very weak hint of parts of the main nebula in a large "S" shaped structure is visible. Although GALEX images show many reflection ghost images, the detection of the lobes in the GALEX images is convincing as the features are neither in the mirroring direction along the optical axes from other bright sources, nor are they in the image of the same telescope pointing as YY Hya. They also resemble in basic shape and location the outer nebulae

seen in the optical images. The $FUV/NUV \gg 1$ suggests similar physics of shocked gas like found in the 4 pc wide blue ring nebula around TYC 2597-735-1 (Hoadley et al. 2020).

2.3. Optical and Infrared Photometry

The light curve data from the Catalina Real-time Transient Survey CRTS (Drake et al. 2009) were downloaded from the online data base⁷ and converted to the solar system barycentric time frame. Additionally, we obtained the time-series photometry from the Gaia DR2 data base (Holl et al. 2018). The WISE data and a handful of data points available from the Palomar Transient Factory (PTF, Law et al. 2009) were obtained from the NASA/IPAC Infrared Science Archive (IRSA)⁸.

Furthermore, we loaded the Transiting Exoplanet Survey Satellite (TESS, Ricker et al. 2015) full frame images (FFI) of sector 8 (February 2020) and quick-look, early release of calibrated FFIs of sector 35 (February/March 2021) and derived the simple aperture photometry (SAP) flux light curve by using *eleonor* (Feinstein et al. 2019) and our in-house public tool *smurfs*⁹. As the TESS pixels are very large ($21''$), the source is contaminated in the SAP aperture by the slightly brighter star Gaia DR2 5675391264067546624, which has $G = 13^m3697$ and a color $BP - RP = 0^m6597$, very similar to that of YY Hya. Thus, while this data allows a time-series analysis, no absolute calibration of the magnitude and the amplitude is possible. We thus used the red Gaia RP , with nearly the same effective wavelength of the passband (see Appendix Table A.2), to derive the calibration scale factor.

Using the visual band magnitude and color of the star in the Gaia photometry to estimate a spectral class range and the apparent magnitude, the central stellar source in the GALEX DR5 source data base (Bianchi et al. 2012) at the position of YY Hya shows a clear UV excess. In total, the collection of time series spans 16 years and 16 802 periods. A complete summary of the photometry can be found in the Appendix in Table A.1. We searched the time series for periods using an own implementation of the phase-dispersion minimization (PDM, Stellingwerf 1978) algorithm. Global solutions as well as individual blocks

⁷ <http://nsssi.cacr.caltech.edu/DataRelease/>

⁸ <https://irsa.ipac.caltech.edu/frontpage/>

⁹ <https://doi.org/10.5281/zenodo.3768032>

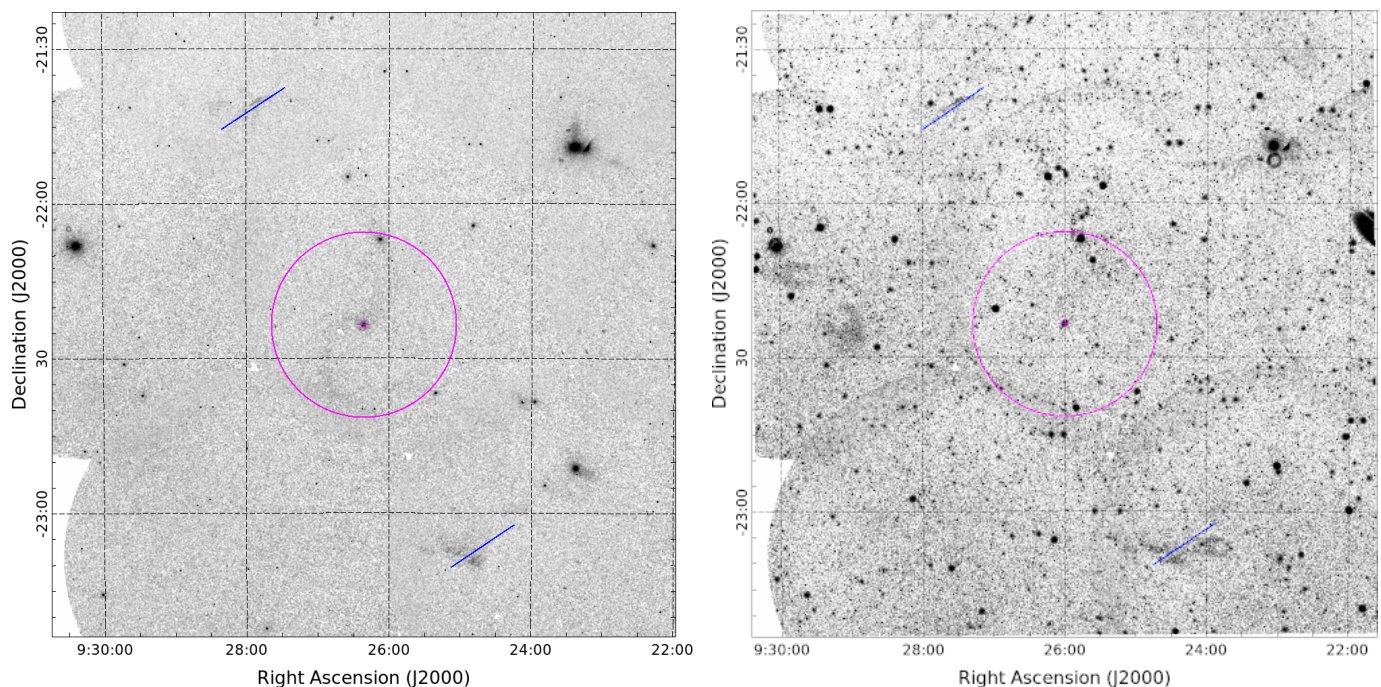


Fig. 4. The GALEX FUV (left) and GALEX NUV (right) composite mosaic image. The 36′ circle and the two 47′ arcs are centered with respect to the position of YY Hya. While the central nebula is not clearly detected, the two vis-à-vis emission lobes are clearly visible in both bands.

of 2 years were obtained to identify possible period changes, but no such changes were found down to the 0.5σ level. The period, $P = 0^d.3347894 \pm 0^d.0000004$ (\equiv to a frequency $f = 2.98695 \text{ d}^{-1}$), is constant to better than 0.1 seconds during those 16 years. Comparing the formalism from [Knigge et al. \(2011\)](#), the resulting limit of the period change implies that the system does not show strong mass transfer at the moment. The PDM is very sensitive to general period changes on those long time series. But as shown for the case of WZ Sge by [Patterson et al. \(2018\)](#), and as discussed in there for a set of other system as well, these stars often show wiggles of the observed-computed (O–C) timing of eclipses, typically on timescales of 10 to 30 years. As we do not see an eclipse in our system, we are not sensitive to such small changes here. The ephemeris of minimum sinusoidal optical light curve is

$$\text{BJD}2458518.5082 + 0.3347894(4)E, \quad (1)$$

where E is the integer cycle count.

Even more surprising is the remarkably sinusoidal shape of the light curve. Fitting a single sine function gives for the TESS data a correlation coefficient of $R^2 \gtrsim 0.9997$ and $rms = 0^m.0073$. The near-perfect sinusoidal light curve allowed us to normalize the amplitudes from various wavelengths to a common light curve, showing that this perfect sinusoidal behavior was valid throughout the whole data period (Fig. 5). Moreover, after the drop from a flux ratio between maximum and minimum of the optical light curve of 2.5 for the two blue bands around 500 nm to 2.2 at 600 nm the amplitude is fairly well linear with a very small slope from 2.2 to 1.95 from approximately 610 to 4600 nm. As the flux in the Rayleigh–Jeans approximation part of a spectrum depends linearly on temperature T , this suggests that the variability originates mostly from temperature changes similar to those found in irradiated systems ([Schaffenroth et al. 2019](#)). Near infrared (NIR) data obtained at two epochs by the Deep Near Infrared Southern Sky Survey (DENIS, [Epchtein et al. 1997](#)) and one epoch from the Two Micron All Sky Survey (2MASS, [Skrut-](#)

[skie et al. 1997](#)) exist. All were obtained at phases near minimum. Using the linear relation of the amplitude with wavelength from the data with existing light curve small corrections towards an estimated minimum light were obtained to be used for the SED based on ATLAS9 stellar atmospheres ([Castelli & Kurucz 2003](#)) later. As the NIR observations were obtained near minimum such an estimate for observations at maximum light would be too much of an extrapolation. Thus we did not use the NIR photometry for the SED during maximum. The filter definitions and the calibration zero points for the entire photometric data are given in the Appendix in Table A.2.

Using the newest 3D Galactic extinction map *Bayestar2019* ([Green et al. 2019](#)) we derive an interstellar reddening as low as $E(B - V) = 0^m.02$ while the *Stilism* map ([Lallement et al. 2019](#)) gives a value of $E(B - V) = 0^m.043 \pm 0^m.17$. We thus adopt the mean value of $0^m.032$ for our further investigations. Furthermore, the extinction curve by [Cardelli et al. \(1989\)](#) was adopted. This covers purely the extinction of the foreground and the environment. Possible internal extinction within the system itself cannot be detected that way.

2.4. Optical Spectra

We obtained spectra of YY Hya at the 2.4 m Hiltner telescope at the MDM Observatory at Kitt Peak, Arizona, using the Ohio State Multi-Object Spectrograph (OSMOS; [Martini et al. 2011](#)). A 1′′.4 slit and a blue grism yielded a resolution of $R \approx 1600$ and a wavelength coverage from 3975 to 6865 Å. For wavelength calibration we used Hg, Ne, and Ar comparison lamps and fine-tuned the wavelength scale using night-sky emission features as needed. We observed spectrophotometric standard stars for flux calibration. Reductions were accomplished using an own pipeline that included elements from astropy and IRAF/pyraf. We also obtained a few spectra with the 1.3 m McGraw-Hill telescope and modspec spectrograph. These had a poorer signal-to-

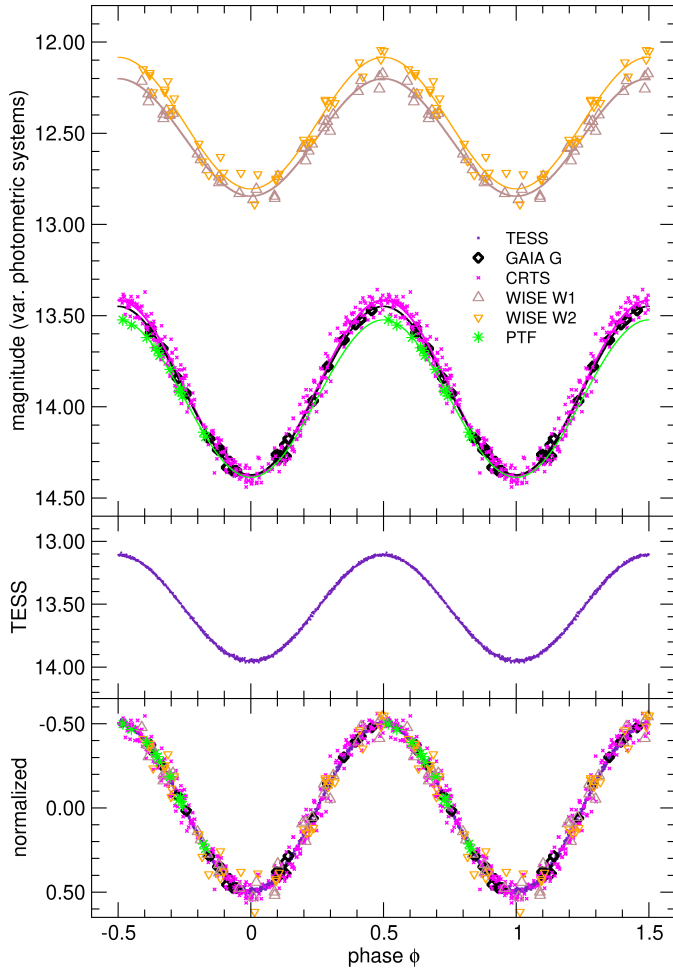


Fig. 5. The light curve taken at various facilities using the period $0^d3347894$. Upper panel: light curves of the CRTS survey, the PTF facility, WISE and Gaia have absolute calibrations. Middle panel: the TESS light curve cannot be calibrated absolutely (see text). Lower panel: all light curves normalized to unity amplitude.

noise ratio than the 2.4 m data, but were consistent with the results.

Table 1 summarizes the observations. A few spectra were taken on three successive nights in 2020 December, all of them near maximum in the optical light curve (the period is so close to 1/3 day that observations on successive nights near meridian transit are at nearly the same phase). In 2021 February and March we obtained much more extensive data on more widely separated nights, which sampled the entire orbit.

In the upper panel of Fig. 6 the averages of the flux-calibrated OSMOS spectra from near maximum and minimum in the optical light curve are plotted on the same scale. The maximum-light spectrum is dominated by a strong blue continuum and numerous emission lines of H, He I, He II and weaker features that appear to be mostly singly and doubly-ionized C and N. The latter are very narrow while the H and He lines appear to be Stark broadened.

This kind of mixture of wide and strong H and He lines combined with narrow emission lines of low-ionized CNO elements looks very much like that in spectra found in post common envelope pre-cataclysmic variables like EC 11575-1845 (= TW CrV), V664 Cas (the central star of the planetary nebula HFG 1, Exter et al. 2005), HS 1857+5144 (Aungwerojwit et al. 2007; Shimansky et al. 2009), BE UMa (Shimansky et al. 2008), NN Ser (the central star of the PN G068.1+11.0, Parsons

Table 1. Journal of Spectroscopic Observations obtained with the OSMOS spectrograph (O) at the 2.4 m Hiltner telescope and with the modspec instrument (X) at the 1.3 m McGraw-Hill telescope.

Start (U.T.)	Instr.	HA start (hh:mm)	HA end (hh:mm)	exp. (s)	N_{exp}
2020-12-15 11:10	O	−00:05	+00:26	600	3
2020-12-16 10:42	O	−00:30	+00:11	1200	2
2020-12-17 11:03	O	−00:05	+00:28	2000	1
2021-02-07 05:47	O	−01:56	+01:55	1000	13
2021-02-09 04:34	O	−03:01	+00:50	1000	13
2021-03-07 03:46	O	−02:07	+02:03	1000	14
2021-03-11 05:40	X	+00:03	+02:04	1800	4
2021-03-12 05:41	X	+00:08	+00:38	1800	1

et al. 2010; Mitrofanova et al. 2016). However, the emission-to-continuum line contrast is much weaker in those objects than the one we find here. Also, they all show spectra signatures of a white dwarf companion in the optical and have late M-type star companions (except BE UMa, Shimansky et al. 2008). UU Sge, also belonging to that class of objects, shows predominately much higher ionization levels for the CNO elements in the spectra (Wawrzyn et al. 2009).

In Table B.1 in the Appendix a full listing including relative line strengths of the very rich emission spectrum at phase 0.5 is given. The minimum-light spectrum is much fainter overall, with much weaker emission lines and prominent absorption features of a late-type star.

To quantify the contribution of the late-type star, we used a set of spectra of late-type stars classified by Keenan & McNeil (1989), observed with the modspec. Using an interactive program we scaled various spectra from this set and subtracted them from the minimum-light spectra, varying the spectral type and scale factor to optimize the cancellation of the late-type absorption features. The lower panel of Fig. 6 shows the best result, obtained with a K2 V star. Stars within ± 2 subclasses of this gave acceptable cancellations.

We measured radial velocities of the late-type star using the IRAF fxcor task, which implements cross-correlation methods described by Tonry & Davis (1979). As a template, we used the average of 76 spectra of late-type IAU velocity standards that had been shifted to zero apparent velocity before the cross-correlation. Note that in this method the wavelengths of individual features are not measured. Regions around emission lines were masked. The spectra near minimum light gave strong correlations. Near maximum, in which the late-type features were barely visible, the correlations were much weaker and the velocity uncertainties correspondingly larger, but nearly all spectra showed at least some correlation. We also measured the velocity of the H α emission line, using a convolution technique (Schneider & Young 1980); the velocities of the other emission lines were similar.

Figure 7 shows the velocities folded with the photometric phase. The emission lines move nearly in phase with the absorption, but with a somewhat smaller velocity amplitude. Table 2 gives the parameters of the best fitting sinusoids of the form $v(t) = \gamma + K_{\text{em,abs}}^i \sin[2\pi(t - T_0)/P]$, so that T_0 corresponds to inferior conjunction of the moving object. The period was held fixed at the photometric value, which spans a much longer time base; the epochs T_0 were allowed to vary. Even with this, both the epochs in Table 2 align with the ephemeris in Eqn. 1 to within 0.01 cycles. Equation 1 is for minimum light. The velocities therefore indicate an irradiation effect, since the cool star's

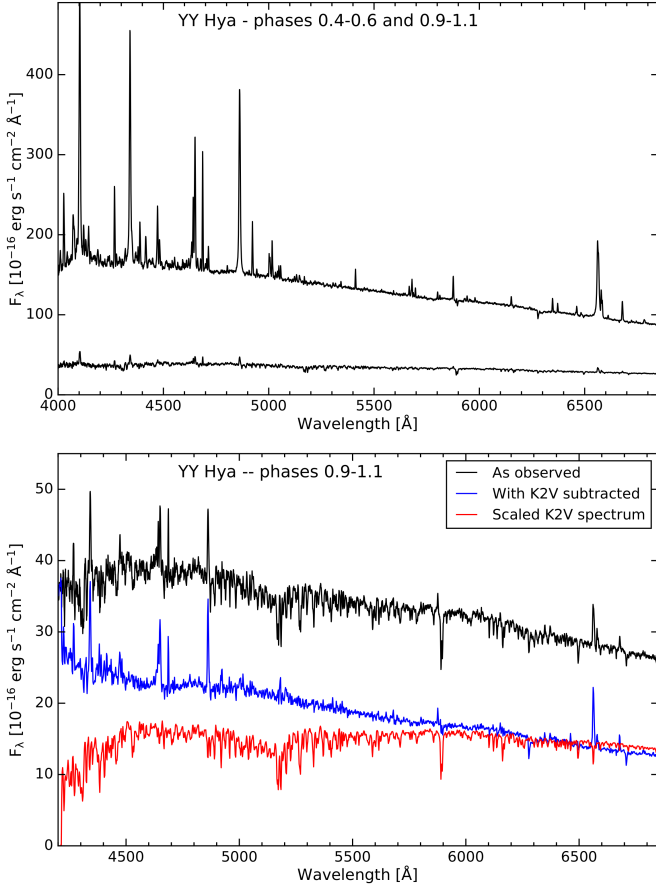


Fig. 6. *Upper panel:* mean OSMOS spectra from 2021 February and March; the top trace is the average of spectra taken near maximum light, and the bottom trace near minimum light. The vertical axis is the same for both traces. *Lower panel:* the upper, black trace shows the same minimum-light spectrum as the top trace. The red trace is a scaled spectrum of a K2 V star, while the blue trace results from subtracting the scaled K-type spectrum from the observed spectrum.

Table 2. Radial velocities derived from the H α emission (em) and from numerous absorption lines (abs). The period was fixed to 0^d3347894. 44 out of the 45 spectra from 2021 were usable.

Data	T_0 BJD -2400000	$K_{\text{em,abs}}^i$ [km s ⁻¹]	γ [km s ⁻¹]	σ [km s ⁻¹]
em	59254.712(2)	105(5)	18(3)	18
abs	59254.708(3)	123(7)	30(4)	21

heated face is maximally turned away from us at inferior conjunction.

In Figs. 8 and 9, we present phase-resolved spectra similar to those produced by trailing a star along a spectrograph slit. To make these, we divided the phase into 100 bins, and for each bin averaged the spectra near that phase using a narrow Gaussian window. The spectra were then formed into a two-dimensional image, repeating once for continuity. In Fig. 8, we used the flux-calibrated spectra; the colormap is set to bring out the details of the spectrum near maximum light (phase 0.5 and 1.5) and the spectrum near minimum light is invisible. Because the light curve is generally extremely regular, the finer-scale horizontal banding is almost certainly an artifact of difference in the flux calibration caused by, for example, thin cloud or variable seeing.

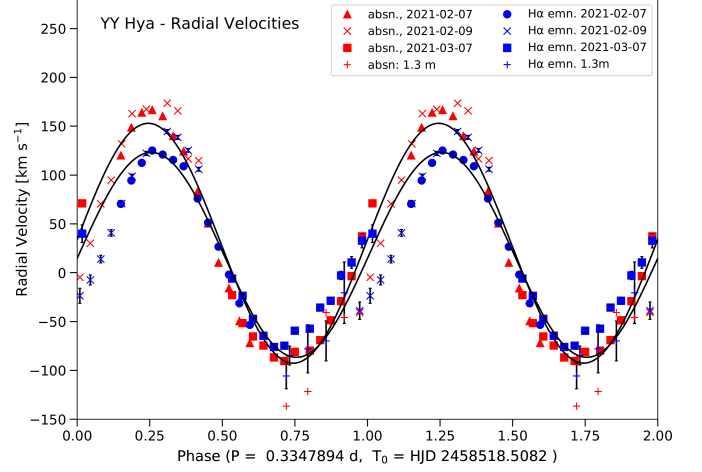


Fig. 7. Radial velocities of the absorption component and H α emission line in YY Hya, as a function of the period and epoch derived from the photometry. To preserve continuity, the data are repeated for one cycle. The solid lines show the best-fitting sinusoids.

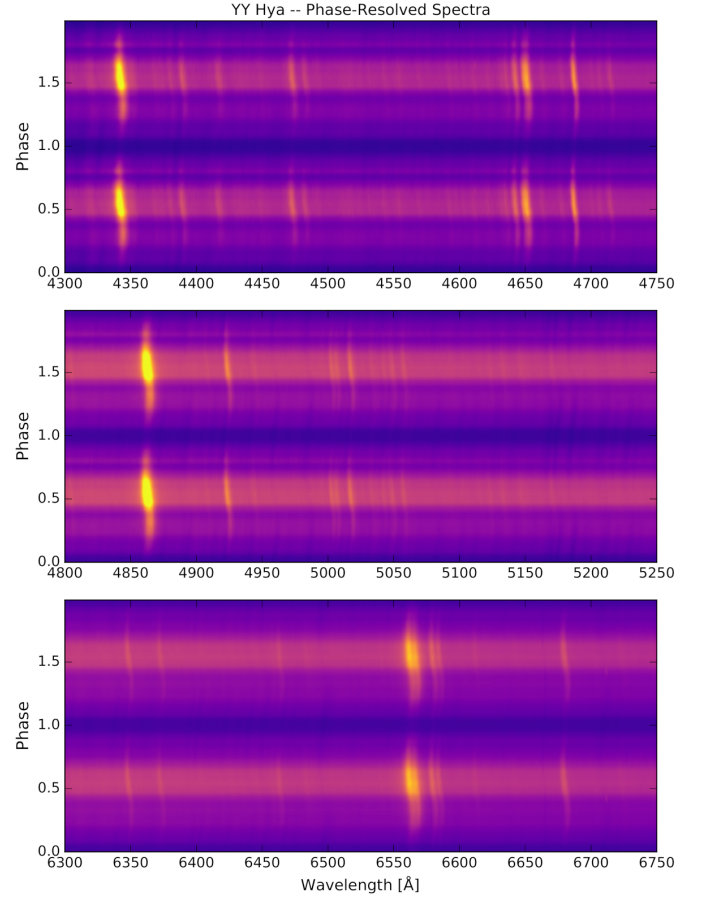


Fig. 8. Two-dimensional phase-resolved spectrum prepared as described in the text. The spectra used here are flux-calibrated.

The emission lines dominate this view, and their velocity variation is evident.

In Fig. 9, the original spectra were divided by their continua, suppressing the overall modulation but bringing up the spectra in the faint phase. Here, the numerous K-star absorption lines can be seen, also moving approximately with the emission, as seen also in the radial velocity graphs (Fig. 7).

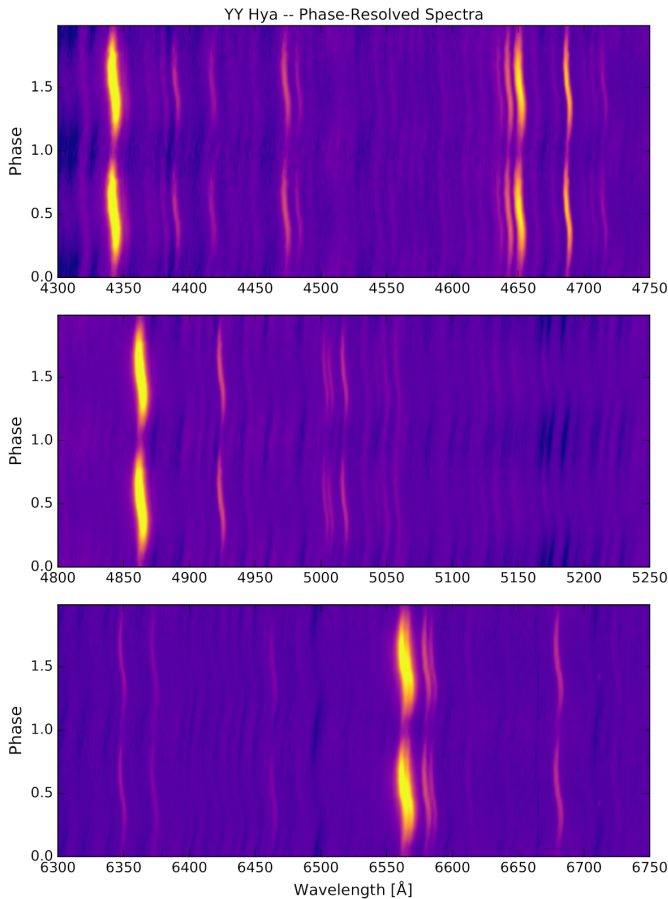


Fig. 9. Two-dimensional phase-resolved spectrum prepared as described in the text. The spectra used here are divided by the continuum.

3. Proposed Binary Model

The photometric modulation and the time-resolved spectra show conclusively that YY Hya is a binary system in which a late-type star is strongly irradiated by a much hotter companion. This, together with the UV excess, leads us to model the system as a compact binary system with a white dwarf (WD) causing the strong irradiation effects. Other than in the objects of the BE UMa family (see e.g. Shimansky et al. 2016), the WD is not luminous enough to contribute significantly or even to dominate the optical luminosity. The resulting WD, although providing more than 99.5% of the flux in the GALEX FUV band, contributes less than 1% in the optical even during minimum phase, when only the non-illuminated side of the K star is seen. The irradiation modelling here follows widely the methods and discussions in Hamilton-Drager et al. (2018) for the post-nova V723 Cas.

While the far side of the secondary star is near the state of the normal main-sequence star, the other side is strongly illuminated and heated. This causes the sinusoidal light curve. Such compact systems are normally in bound rotation (see e.g. Schandl et al. 1997). The recurrent nova CI Aql, although even a bit more massive and with a period of > 0.6 a significantly larger system behaves perfectly like this as well (Lederle & Kimeswenger 2003). Similar results are found by Haefner et al. (2004) and Parsons et al. (2010) in the case of the pre-cataclysmic variable NN Ser. The latter authors write in their analysis of the light curve that there is no detectable heating of the unirradiated face, despite intercepting radiative energy from the white dwarf which

exceeds its own luminosity by over a factor of 20.0. Assuming now a nearly constant temperature at the far side of the cold stellar component, together with the findings in the spectroscopy (Fig. 6), we obtained an initial guess for the system during minimum. The lack of an eclipse gives an upper boundary for the system inclination, which only marginally depends on the mass ratio q .

As a hot compact companion does not suffer any deformation or irradiation effects, and as it is visible always, it can be modelled as constant contribution independent from the phase. This is especially important for the GALEX FUV band, where the large secondary star does not contribute to the radiation anymore, and thus no variation is expected at all.

Using the updated online version¹⁰ of the compilation and calibration by Pecaut & Mamajek (2013) we obtain then an upper limit of $M_* \leq 0.8 M_\odot$ and an radius $R_* \approx 0.75 R_\odot$. The effective temperature then would be $T_* \leq 5000$ K. This corresponds to the spectroscopy during minimum phase shown above. However the 0.7 to $5 \mu\text{m}$ photometric colors during the minimum phase suggest a temperature of more likely near to 4000 K. That would correspond to a K6-7 star with $M_* \approx 0.6 M_\odot$, $R_* \geq 0.63 R_\odot$ and $T_* \geq 4000$ K. We attribute the difference to the fact, that always a small fraction of the slightly heated transition zone towards the illuminated surface will show spectral lines resembling those of a slightly hotter star than that one found in the near- and mid-infrared photometry. Due to the inclination of the system here, other than in case of NN Ser, we always are contaminated by some light from the hotter illuminated side. This is supported by the distance estimate obtained from Gaia eDR3. The sole K2V star, without additional illuminating effect, with the given magnitudes during minimum, would lie already at > 500 pc. However the inclination always makes some additional flux from the illuminated side contributing to the photometry even during minimum. This effect diminishes towards the red and infrared (see also the decomposition in Fig. 6).

The mass M_{WD} of the compact companion and the ratio q finally is defined by the orbital period P , the system inclination i and the velocity half amplitude K from our spectroscopy by the binary mass fraction

$$f = \frac{M_{\text{WD}}^3 \sin^3 i}{(M_{\text{WD}} + M_*)^2} = \frac{P K^3}{2\pi G} \quad (2)$$

where G is gravitational constant, resulting in $0.4 \leq M_{\text{WD}} \leq 1.2 M_\odot$.

To model the light curve in detail we used the program *Binary Maker 3* (BM3, Bradstreet & Steelman 2002)¹¹. As mentioned already and nicely shown in the case of the evolution of the post-nova V723 Cas over the years moving to a low quiescence state, strong mass transfers and accretion discs cause significant asymmetric structures in the light curves (Hamilton-Drager et al. 2018). However, as we have a perfect sinusoidal light curve, we are able to assume a system without an accretion disk here for our model. As discussed in detail by Heber et al. (2018), irradiation efficiency is not completely understood and thus a source of systematic uncertainty. Schaffenroth et al. (2019) showed in the Eclipsing Reflection Effect Binaries from Optical Surveys (EREBOS) project with a large sample of spectroscopically investigated compact binary systems with hot subdwarf (sdB) companions that the efficiency in such systems is near to complete absorption of the UV radiation by the secondary. Model atmospheres using the PHOENIX model atmo-

¹⁰ <http://www.pas.rochester.edu/~emamajek>

¹¹ <http://www.binarymaker.com/>

sphere code for the M-type stars of the non-mass-transferring post-common-envelope binaries GD 245, NN Ser, AA Dor, and UU Sge show similar results (Barman et al. 2004). Thus we adopted a unity value here.

A stochastic gradient descent method (Russell et al. 2010) led to various local solutions in the minimum χ^2 search in the multidimensional parameter space. Therefore we manually calculated a complete grid of light curves with inclinations varying for each mass within the above calculated range in steps of 1° and a variation of the mass $0.4 \leq M_{\text{WD}} \leq 1.2 M_\odot$ in steps of $0.05 M_\odot$. The size R_{MS} of the secondary was varied from $\approx 80\%$ to exactly 100% of the Roche Lobe R_{RL} in 12 steps. However, only within a few percent below the Roche Lobe perfect sinusoidal light curves were obtained. The temperature of the compact companion was varied from 50 000 to 80 000 K. Then the luminosity of the compact star was adapted until the light curve amplitude in the TESS and the CRTS bands was recovered as observed at a phase interval of ± 0.05 around minimum and maximum ($\phi_{\text{MIN}} = 0.0$ and $\phi_{\text{MAX}} = 0.5$) each time. As the TESS photometric band is fairly red, this modelling does not suffer from the strong emission line regions at wavelengths below 5500 Å. As next step the goodness of the fit was calculated for the remaining phase regions by

$$\sum \frac{(I_{\text{data}} - I_{\text{model}})^2}{|I_{\text{model}}|} \quad \forall (0.05 < \phi < 0.45) \vee (0.55 < \phi < 0.95).$$

The phase restriction for this calculation was used to avoid a dependency from the fit of the amplitude in the step before. A small sub-sample of the residuals ($I_{\text{data}} - I_{\text{model}}$) of the light curves is shown in the appendix in Fig. C.1. Purely from photometry there is only one possible solution in inclination i for each temperature T_{WD} and luminosity L_{WD} for each of the selected M_{WD} . Due to the nearly noise-free TESS light curve this is very sensitive to the inclination i . Thus around the preliminary solution the grid was refined to 0.1 degree steps. The bandwidth of solutions varies only from 36 to just above 40° as function of the WD mass (Fig. 10). The system parameters, however, give us then a radial velocity. For an illuminated star we have to expect that the emission lines originate only from the half of the star inwards to the mass center. Thus the observed velocity half-maximum $K_{\text{em}}/\sin(i)$ of the emission lines will underestimate the orbital velocity K from Eqn. 2. On the other hand the absorption lines originate from the weakly and unilluminated part, having its weighted center outside the mass center. Thus the $K_{\text{abs}}^i/\sin(i)$ from the absorption lines will be an overestimate. This is described also in detail for EC 11575-1845 and V664 Cas in Exter et al. (2005). We thus safely and very conservative may use those two extreme cases $K_{\text{em}}/\sin(i)$ and $K_{\text{abs}}^i/\sin(i)$ as lower and upper boundaries, respectively. As indicated in Fig. 10 this limits the mass range for the white dwarf to $0.64 < M_{\text{WD}} < 0.85 M_\odot$ with favorite mass of $M_{\text{WD}} \approx 0.725 M_\odot$. The distance of the compact companion was then derived as well. The latter varies the luminosity in the mass-temperature plane (Fig. 11). However, the above mass constraints limit our further steps of the investigation to a small region in the luminosity-mass-temperature plane.

The luminosity L_{WD} and the effective temperature T_{WD} were *a priori* independent free parameters, but are linked to a single degree of freedom by the GALEX FUV flux and the known distance of the system. For this purpose all WDs with $T > 50\,000$ K in the sample of Finley et al. (1997) where GALEX FUV measurements were available were used together with the new Gaia eDR3 distances to derive a relationship between those two parameters. For the GALEX photometry the entire model

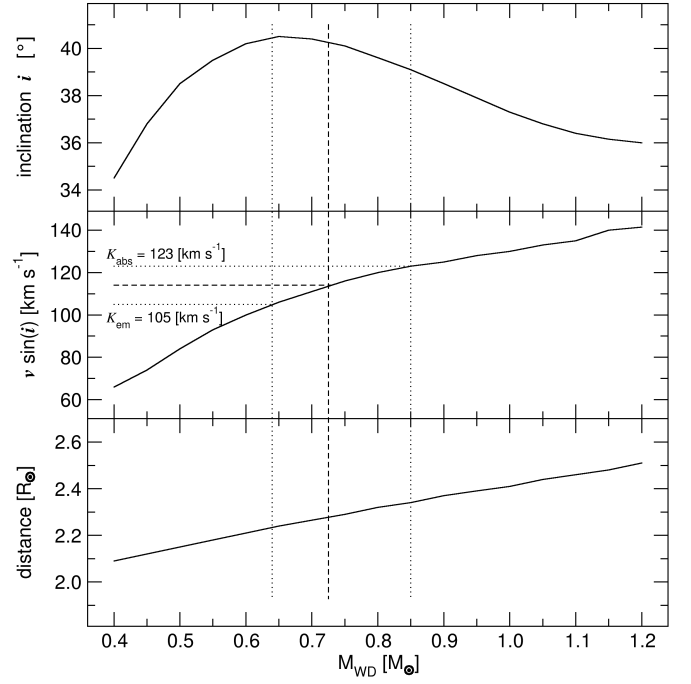


Fig. 10. The resulting best-fit model as function of the mass of the white dwarf. The inclination i of the system (top), the resulting K half velocity amplitude (middle) and the orbital separation of the mass centers of the stars (bottom panel). The dashed line marks the average between the extreme cases of the emission and the absorption line velocities, while the dotted lines mark the two extreme cases (see text).

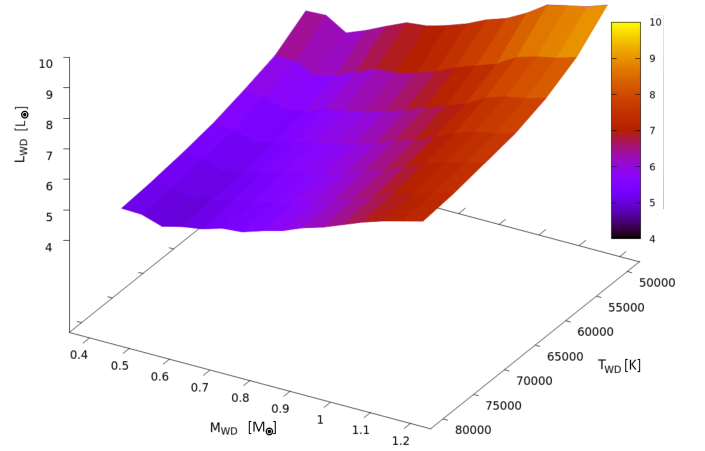


Fig. 11. The solution plane for the luminosity L_{WD} as function of the mass and the effective temperature of the white dwarf for the complete model grid. The luminosity is colour-coded as well for clarification.

grid from $50\,000 < T < 150\,000$ K; $5.0 < \log(g[\text{cgs}]) < 8.0$ from Rauch (2003) was downloaded and folded with the published GALEX FUV filter curve (Rodrigo et al. 2013). However, as the dependency on gravity $\log(g)$ is very small in our temperature range this dimension was ultimately neglected. We used for the absolute calibration the two hot WD stars 0004+330 ($T_{\text{eff}} = 85\,000$ K) and 0231+050 ($T_{\text{eff}} = 50\,000$ K) from the calibration sample for GALEX by Camarota & Holberg (2014) and the WD in NN Ser due to its very accurately known stellar radius (Haefner et al. 2004; Parsons et al. 2010). Although the statistical errors given for the GALEX data are very small, we used a conservative error estimate, caused from possible systematic error in the extinction correction A_{FUV} of 50%. This leads us to the

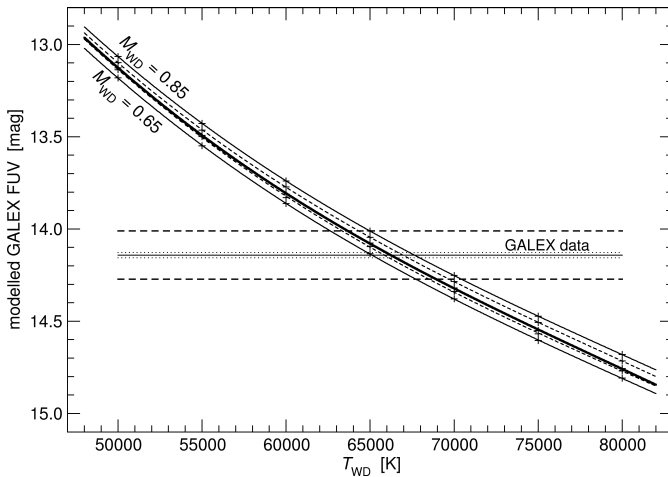


Fig. 12. The best model magnitude. The solution for the mass range defined from the velocities. The GALEX measurement error (dotted lines) are very small. Conservative estimates for systematic errors are indicated by the thick dashed lines.

Table 3. Parameters of the best model.

MS star mass	M_*	0.62	± 0.05	M_\odot
MS star radius	R_*	94%	$+2\%$ -3%	R_{RL}
MS star temperature	T_*	4.5	± 0.3	kK
MS star luminosity ^a	L_*	0.18	$+0.03$ -0.04	L_\odot
WD mass	M_{WD}	0.725	$+0.12$ -0.07	M_\odot
WD radius	R_{WD}	0.019	$+0.004$ -0.003	R_\odot
WD temperature	T_{WD}	66.5	± 3.5	kK
WD star luminosity ^b	L_{WD}	5.2	± 1.5	L_\odot
absorption efficiency ^c	η	1.0		
system inclination	i	40.2°	$\pm 0.8^\circ$	

^(a) The luminosity of the MS star was calculated from mass and Roche Lobe radius without taking into account other possible systematic effects.

^(b) The luminosity of the WD star is constrained by the light curve amplitude. Thus error bars of the other parameters are not independent.

^(c) adopted value

final temperature range $T_{\text{WD}} = 66\,500 \pm 3500$ K (Fig. 12). The best model parameters are summarized in Table 3 and Fig. 13 shows the resulting geometry together with the light curve.

4. Galactic Context

Together with our spectroscopy, the Gaia mission data allow us to derive a full 6D dynamical investigation of the source. We use the Gaia EDR3 parallax and proper motions, and the average of γ derived from the emission and the absorption lines as system radial velocity with a conservative error estimate due to the scatter in Fig. 7 (see Table 2). For the latter we thus use $v_{\text{rad}} = 24 \pm 10$ km s⁻¹. We use the Galactic potential as described by Allen & Santillan (1991) with the code of Odenkirchen & Brosche (1992) to compute the Galactic orbit and kinematic parameters of YY Hya in analogy to Pauli et al. (2006).

The orbit in the Cartesian Galactic coordinate frame X , Y , Z with the Galactic center at the origin and ρ parameterizing the Galactocentric distance (Fig. 14) is nearly circular and bound to

the Galactic disk. Moreover, the comparison with the local WD sample by Pauli et al. (2006) also show that the position of the radial versus the rotational velocity components and the angular component J_z perpendicular to the disk versus the orbital eccentricity e clearly puts YY Hya into the middle of the young thin disk population. The currently reached height $Z = 155$ pc above the disk plane is in fact close to the maximum elevation reached in orbit.

Consequently, we are able to use the metal-rich WD evolution tracks from the most recent calculations by Miller Bertolami (2016) for the WD component of YY Hya. The WD mass of $0.725 M_\odot$ gives us with the initial-to-final mass relation of Cummings et al. (2018) an initial stellar mass of 3–4 M_\odot . As the progenitor thus was a late B-type star (Mowlavi et al. 2012; Eker et al. 2018; Serenelli et al. 2021) with a lifetime of approximately half a Gyr or slightly below that, we conclude that the K-star companion has barely evolved off the zero-age main sequence.

Acknowledgements. We would like to thank the referee Steve Howell very much for his ideas for improving the original work. This research has made use of NASA’s Astrophysics Data System Bibliographic Services (ADS), use of the SVO Filter Profile Service supported from the Spanish MINECO through grant AYA2017-84089, NASA/IPAC Infrared Science Archive (IRSA), which is funded by the National Aeronautics and Space Administration and operated by the California Institute of Technology, and use of the SIMBAD database (Wenger et al. 2000), operated at CDS, Strasbourg, France. Furthermore this research made use of the Stellarium software (stellarium.org) version 0.19.1. and of the astrometry.net project, which is partially supported by the US National Science Foundation, the US National Aeronautics and Space Administration, and the Canadian National Science and Engineering Research Council. The CSS survey is funded by the National Aeronautics and Space Administration under Grant No. NNG05GF22G issued through the Science Mission Directorate Near-Earth Objects Observations Program. The CRTS survey is supported by the U.S. National Science Foundation under grants AST-0909182 and AST-1313422. This publication makes use of data products from the Wide-field Infrared Survey Explorer (WISE), which is a joint project of the University of California, Los Angeles, and the Jet Propulsion Laboratory/California Institute of Technology, funded by the National Aeronautics and Space Administration. The Intermediate Palomar Transient Factory (PTF) project is a scientific collaboration among the California Institute of Technology, Los Alamos National Laboratory, the University of Wisconsin, Milwaukee, the Oskar Klein Center, the Weizmann Institute of Science, the TANGO Program of the University System of Taiwan, and the Kavli Institute for the Physics and Mathematics of the Universe. The MDM Observatory is operated by Dartmouth College, Columbia University, Ohio State University, Ohio University, and the University of Michigan. This work presents results from the European Space Agency (ESA) space mission Gaia. Gaia data are being processed by the Gaia Data Processing and Analysis Consortium (DPAC). Funding for the DPAC is provided by national institutions, in particular the institutions participating in the Gaia MultiLateral Agreement (MLA). The Gaia mission website is <https://www.cosmos.esa.int/gaia>. The Galaxy Evolution Explorer (GALEX) is a NASA Small Explorer. We gratefully acknowledge NASA’s support for construction, operation, and science analysis for the GALEX mission, developed in cooperation with the Centre National d’Etudes Spatiales of France and the Korean Ministry of Science and Technology. This paper includes data collected by the TESS mission. Funding for the TESS mission is provided by the NASA Explorer Program.

References

- Allen, C. & Santillan, A. 1991, *Rev. Mexicana Astron. Astrofis.*, 22, 255
- Aungwerojwit, A., Gänsicke, B. T., Rodríguez-Gil, P., et al. 2007, *A&A*, 469, 297
- Barman, T. S., Hauschildt, P. H., & Allard, F. 2004, *ApJ*, 614, 338
- Barria, D., Kimeswenger, S., Kausch, W., & Goldman, D. S. 2018, *A&A*, 620, A84
- Bertin, E. & Arnouts, S. 1996, *A&AS*, 117, 393
- Bianchi, L. 1999, *Mem. Soc. Astron. Italiana*, 70, 365
- Bianchi, L., Herald, J., Efremova, B., et al. 2012, *VizieR Online Data Catalog*, II/312
- Boyce, E. H. 1936, *Harvard College Observatory Bulletin*, 903, 28
- Bradstreet, D. H. & Steelman, D. P. 2002, in *American Astronomical Society Meeting Abstracts*, Vol. 201, American Astronomical Society Meeting Abstracts, 75.02

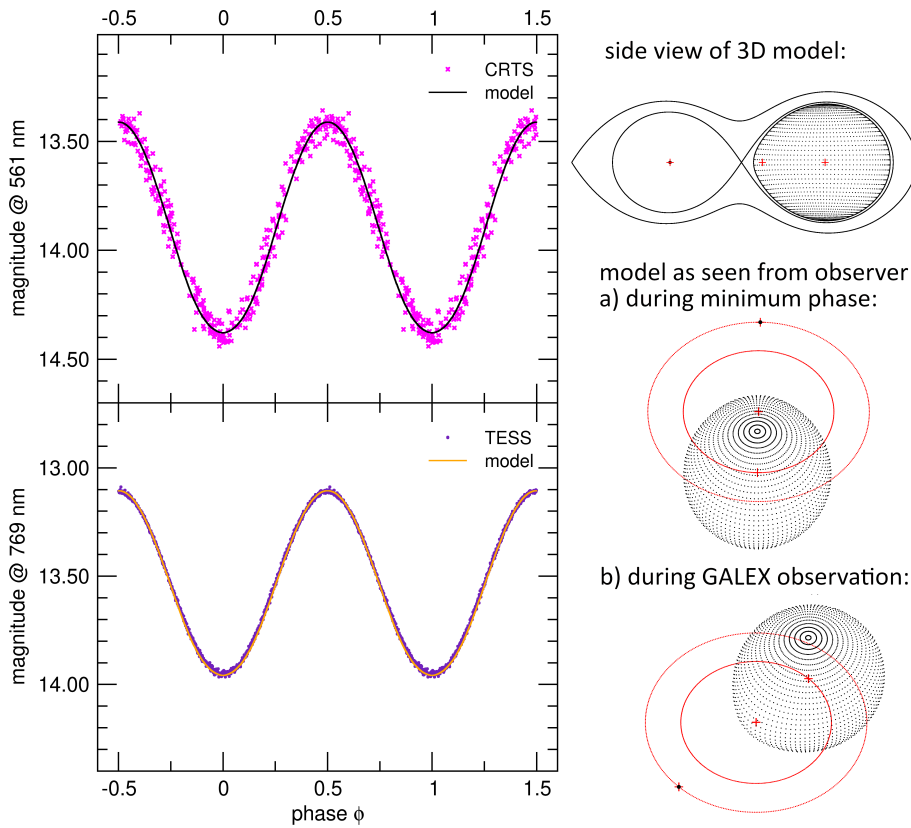


Fig. 13. The BM3 model. The best fit model based on the red passband TESS data and then calculated for the shorter wavelength CRTS data to constrain the temperatures of the components by the higher amplitude in the visual wavelength. The drawings (from top to bottom) show the side view including the Roche lobe limit, the model at minimum phase showing mainly the cold side of the MS star, and the phase during the GALEX observations showing nearly the whole hot side. The crosses mark the mass centers of the stars and the system barycenter. The red ellipses are the projected orbits.

- Camarota, L. & Holberg, J. B. 2014, *MNRAS*, 438, 3111
- Cardelli, J. A., Clayton, G. C., & Mathis, J. S. 1989, *ApJ*, 345, 245
- Castelli, F. & Kurucz, R. L. 2003, in *IAU Symposium*, Vol. 210, *Modelling of Stellar Atmospheres*, ed. N. Piskunov, W. W. Weiss, & D. F. Gray, A20
- Catelan, M., Pritzl, B. J., & Smith, H. A. 2004, *ApJS*, 154, 633
- Cummings, J. D., Kalirai, J. S., Tremblay, P. E., Ramirez-Ruiz, E., & Choi, J. 2018, *ApJ*, 866, 21
- Dambis, A. K., Berdnikov, L. N., Kniazev, A. Y., et al. 2013, *MNRAS*, 435, 3206
- Drake, A. J., Djorgovski, S. G., Catelan, M., et al. 2017, *MNRAS*, 469, 3688
- Drake, A. J., Djorgovski, S. G., Mahabal, A., et al. 2009, *ApJ*, 696, 870
- Eker, Z., Bakış, V., Bilir, S., et al. 2018, *MNRAS*, 479, 5491
- Epchtein, N., de Batz, B., Caproni, L., et al. 1997, *The Messenger*, 87, 27
- Exter, K. M., Pollacco, D. L., Maxted, P. F. L., Napiwotzki, R., & Bell, S. A. 2005, *MNRAS*, 359, 315
- Feinstein, A. D., Montet, B. T., Foreman-Mackey, D., et al. 2019, *PASP*, 131, 094502
- Finley, D. S., Koester, D., & Basri, G. 1997, *ApJ*, 488, 375
- Gaia Collaboration, Brown, A. G. A., Vallenari, A., et al. 2018, *A&A*, 616, A1
- Gao, X.-H. 2016, *Research in Astronomy and Astrophysics*, 16, 184
- Green, G. M., Schlafly, E., Zucker, C., Speagle, J. S., & Finkbeiner, D. 2019, *ApJ*, 887, 93
- Guthnick, P. & Prager, R. 1936, *Astronomische Nachrichten*, 260, 393
- Haefner, R., Fiedler, A., Butler, K., & Barwig, H. 2004, *A&A*, 428, 181
- Hambly, N. C., MacGillivray, H. T., Read, M. A., et al. 2001, *MNRAS*, 326, 1279
- Hamilton-Drager, C. M., Lane, R. I., Recine, K. A., et al. 2018, *AJ*, 155, 58
- Heber, U., Irrgang, A., & Schaffenroth, J. 2018, *Open Astronomy*, 27, 35
- Hind, J. 1845, *The London, Edinburgh, and Dublin Philosophical Magazine and Journal of Science*, 27, 416
- Ho, P. Y. 1962, *Vistas in Astronomy*, 5, 127
- Hoadley, K., Martin, D. C., Metzger, B. D., et al. 2020, *Nature*, 587, 387
- Holl, B., Audard, M., Nienartowicz, K., et al. 2018, *A&A*, 618, A30
- Hsi, T.-T. 1957, *Smithsonian Contributions to Astrophysics*, 2, 109
- Keenan, P. C. & McNeil, R. C. 1989, *ApJS*, 71, 245
- Knigge, C., Baraffe, I., & Patterson, J. 2011, *ApJS*, 194, 28
- Kronk, G. W. 1999, *Cometography: A Catalog of Comets, Volume 1: Ancient-1799* (Cambridge University Press)
- Lallement, R., Babusiaux, C., Vergely, J. L., et al. 2019, *A&A*, 625, A135
- Lang, D., Hogg, D. W., Mierle, K., Blanton, M., & Roweis, S. 2010, *AJ*, 139, 1782
- Law, N. M., Kulkarni, S. R., Dekany, R. G., et al. 2009, *PASP*, 121, 1395
- Lederle, C. & Kimeswenger, S. 2003, *A&A*, 397, 951
- Magrini, L., Perinotto, M., Corradi, R. L. M., & Mampaso, A. 2003, *A&A*, 400, 511
- Martin, D. C., Fanson, J., Schiminovich, D., et al. 2005, *ApJ*, 619, L1
- Martini, P., Stoll, R., Derwent, M. A., et al. 2011, *PASP*, 123, 187
- Miller Bertolami, M. M. 2016, *A&A*, 588, A25
- Mitrofanova, A. A., Shimansky, V. V., Borisov, N. V., Spiridonova, O. I., & Gabdeev, M. M. 2016, *Astronomy Reports*, 60, 252
- Morgan, D. 1995, *IEEE Spectrum*, 6, 25
- Mowlavi, N., Eggenberger, P., Meynet, G., et al. 2012, *A&A*, 541, A41
- Needham, J. 1959, *Science and Civilisation in China: Volume 3, Mathematics and the Sciences of the Heavens and the Earth*, Vol. 3 (Cambridge University Press)
- Odenkirchen, M. & Brosche, P. 1992, *Astronomische Nachrichten*, 313, 69
- Parker, Q. A., Bojčić, I., & Frew, D. J. 2017, in *Planetary Nebulae: Multi-Wavelength Probes of Stellar and Galactic Evolution*, ed. X. Liu, L. Stanghellini, & A. Karakas, Vol. 323, 36–39
- Parker, Q. A., Bojčić, I. S., & Frew, D. J. 2016, in *Journal of Physics Conference Series*, Vol. 728, *Journal of Physics Conference Series*, 032008
- Parsons, S. G., Marsh, T. R., Copperwheat, C. M., et al. 2010, *MNRAS*, 402, 2591
- Patterson, J., Stone, G., Kemp, J., et al. 2018, *PASP*, 130, 064202
- Pauli, E. M., Napiwotzki, R., Heber, U., Altmann, M., & Odenkirchen, M. 2006, *A&A*, 447, 173
- Pecaut, M. J. & Mamajek, E. E. 2013, *ApJS*, 208, 9
- Rauch, T. 2003, *A&A*, 403, 709
- Ricker, G. R., Winn, J. N., Vanderspek, R., et al. 2015, *Journal of Astronomical Telescopes, Instruments, and Systems*, 1, 014003
- Rodrigo, C., Solano, E., & Bayo, A. 2013, *SVO Filter Profile Service Version 1.0*, IVOA Note 10 May 2013
- Russell, S., Russell, S., Norvig, P., & Davis, E. 2010, *Artificial Intelligence: A Modern Approach*, Prentice Hall series in artificial intelligence (Prentice Hall)
- Schaffenroth, V., Barlow, B. N., Geier, S., et al. 2019, *A&A*, 630, A80
- Schendl, S., Meyer-Hofmeister, E., & Meyer, F. 1997, *A&A*, 318, 73
- Schneider, D. P. & Young, P. 1980, *ApJ*, 238, 946
- Serenelli, A., Weiss, A., Aerts, C., et al. 2021, *A&A Rev.*, 29, 4
- Shimansky, V. V., Borisov, N. V., Pozdnyakova, S. A., et al. 2008, *Astronomy Reports*, 52, 558
- Shimansky, V. V., Mitrofanova, A. A., Borisov, N. V., Fabrika, S. N., & Galeev, A. I. 2016, *Astrophysical Bulletin*, 71, 463
- Shimansky, V. V., Pozdnyakova, S. A., Borisov, N. V., et al. 2009, *Astrophysical Bulletin*, 64, 349

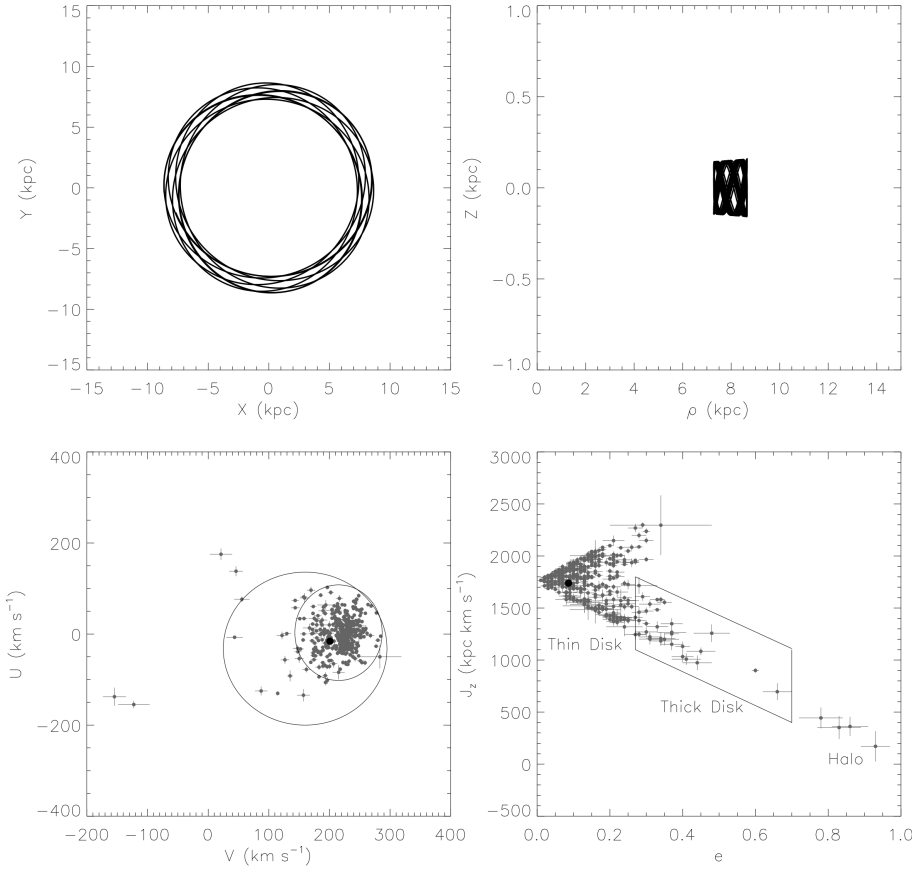


Fig. 14. The kinematics of YY Hya based on our spectroscopic system velocity and the Gaia parallax and proper motions. Upper panels: predicted orbit of YY Hya in the Milky Way for the next 2 Gyrs. Left: orbit projected on the Galactic plane, the Galactic center is at the origin; Right: meridional plot of the orbit. Lower panels - comparison of kinematic properties of YY Hya with the local WD sample by [Pauli et al. \(2006\)](#): Left: the radial velocity component U versus the velocity V in rotational direction, the inner circle encloses the region of thin disk objects, the outer circle the thick disk regime; Right: the angular momentum component J_z perpendicular to the plane versus the orbit eccentricity e .

- Skrutskie, M. F., Schneider, S. E., Stiening, R., et al. 1997, The Two Micron All Sky Survey (2MASS): Overview and Status., Vol. 210 (ASSL), 25
- Stellingwerf, R. F. 1978, ApJ, 224, 953
- Tonry, J. & Davis, M. 1979, AJ, 84, 1511
- Wawrzyn, A. C., Barman, T. S., Günther, H. M., Hauschildt, P. H., & Exter, K. M. 2009, A&A, 505, 227
- Weiler, M. 2018, A&A, 617, A138
- Wenger, M., Ochsenbein, F., Egret, D., et al. 2000, A&AS, 143, 9
- West, R. M. 1974, S&T, 48, 224
- Williams, J. 1871, MNRAS, 32, 32

Appendix A: The photometry data

Table A.1. Time span, passband definition and number of available data points for the photometric observations.

survey	date [UTC]	MJD _{helio}	band	<i>N</i>
CRTS	from 2005-10-11 05:24 to 2013-05-09 23:52	53654.225 56421.995	<i>V</i>	315
WISE	from 2010-05-17 06:05 to 2010-11-28 22:45	55333.254	<i>W1</i>	37
		55528.948	<i>W2</i>	36
PTF	from 2013-03-11 04:22 to 2013-03-12 05:06	56362.182 56363.213	<i>R</i>	12
Gaia	from 2014-11-02 01:12 to 2016-05-02 19:53	56963.050	<i>G</i>	27
		57510.829	<i>BP</i>	27
			<i>RP</i>	27
TESS	from 2019-02-05 00:21 to 2019-02-27 23:52	58519.015 58541.995	<i>R_T</i>	748
	from 2021-02-10 12:02 to 2021-03-06 11:32	59255.501 59279.481	<i>R_T</i>	2665
DENIS	at 1996-04-20 12:48	50193.534	<i>I_cJK_s</i>	
	at 2000-01-24 18:25	51567.768	<i>I_cJK_s</i>	
2MASS	at 1999-02-18 14:54	51227.621	<i>JHK_s</i>	

In Table A.1 the summary for the observations for the time series used in this paper are given. Table A.2 gives an overview of the photometry. Passbands and zero points are taken from the continuously maintained online data base¹² of the SVO filter service (Rodrigo et al. 2013). In case of Gaia, where several filter sets are defined for DR2, we used the revised definition by Weiler (2018) from the data base. The interstellar extinction calculation is based on Cardelli et al. (1989) and the adopted reddening value of $E(B - V) = 0.032$ using $R = 3.1$. As the line of sight is far from the Galactic plane and does not show major dense clouds in the vicinity, these values derived for the thin interstellar matter seem to be most applicable. Due to the small value of the extinction, in fact the selection of the curve type and of R is not causing a significant variation of the result. For those data sets, where a full fit of the light curve was possible, the minimum, mean and maximum from the derived sinusoidal curve fit is used. For the experiments and bands where only one or two measurements were given the phase of the measurement is given together with the magnitude m_{λ}^p . Furthermore we used the wavelength–magnitude relation from the large data time series to calculate an estimate for the minimum brightness and corrected for interstellar extinction leading to $m_{\lambda}^{\min,0}$. Only for the GALEX data no such amplitude correction was derived. As discussed before we do not have to assume a significant amplitude of the the far UV component.

¹² <http://svo2.cab.inta-csic.es/theory/fps/>

Appendix B: The narrow-band image calibration

The image mosaic was obtained from 294 images taken at the CHILESCOPE facilities. CHILESCOPE¹³ is a remotely controlled commercial observatory located in the Chilean Andes (70°45′53″W, 30°28′15″S, 1567 m a.s.l.) about 25 km south of the Gemini South and LSST telescope site Cerro Pachón. We used the two 50cm Newtonian telescopes built by Astro System Austria (ASA)¹⁴. These telescopes have a focal ratio $f/3.8$ and are equipped with 4 K × 4 K FLI PROLINE 16803¹⁵ CCD cameras, yielding a pixel scale of 0.963 pixel^{−1} and a FOV of 1.096 × 1.096. Furthermore, we used for the mosaic the H α (FWHM 3nm) filter from Astrodon¹⁶. This filter is known to suppress contamination from possible [N II] to a level below 5% of the intensity of those lines. As the [N II]:[S II] ratio is about 10:1 in shocked nebulae like supernovae remnants and even lower for H II regions (Magrini et al. 2003; Barría et al. 2018), and as [S II] was not detected in even the brightest regions, we are able to conclude, that we do not suffer from contamination by the nitrogen line.

Each individual exposure time was 20 minutes around 9 pointing positions with their FOV overlapping 50% each. A total exposure time of about 100 hours was accumulated. Due to the overlap the central regions were covered with a total exposure time of 40 hours, while the outer ring with 25% of the image width was covered only by 20 hours. However the very corners were mapped only about 11 hours. To compensate for minor variations due to weather, seeing and airmass, in the overlapping regions a common set of about 300 stars ranging from a 5 σ detection level until the overexposure at the central pixels were extracted using SExtractor v 2.19.5 (2019-07-27) (Bertin & Arnouts 1996). They were used to scale the frames to a common flux calibration. The median of this calibration was used and the *rms* of these calibration factor was about 20%. The worst case was a set of less than 10 frames achieving only about 50% of the median flux. due to the high overlap of up to 120 fields, no special noise suppression handling for those fields after the flux scaling was required.

The astrometry was obtained by the use of a local installation of *solve-field* and *wcs-resample* of the astrometry.net¹⁷ suite v0.85 (Lang et al. 2010) with a Gaia eDR3 catalog subset of the surrounding 3° field. To get a proper distortion correction of this fast $f/3.8$ telescopes a 4th order projection correction prior to stacking the images was required. The final positional *rms* was below 1/5th of a pixel. Resampling to this grid allowed to generate a mean image now. At each position now the image count varies from 32 to 120 frames. We used the mean value of the pixels, eliminating the 3 lowest and 3 highest values. This removed cosmics and satellite spurs but still reduces noise by building means of a large number of frames. Thus it is superior to simply using the median value.

Lacking calibrator and standard fields in the used H α filter set, Gaia data were used to derive an absolute flux estimation. About 1000 stars from the central region just outside of the main nebula and from the NE and the SW corner field were matched with Gaia eDR3 stars. The red band magnitudes Gaia *RP* and the *BP - BR* color were used to derive the zero point *ZP* and a linear color term

¹³ <http://www.chilescope.com/>

¹⁴ <https://www.astrosysteme.com/>

¹⁵ <https://www.flicamera.com/>

¹⁶ <https://astrodon.com/>

¹⁷ <http://astrometry.net/>

Table A.2. Overview of the photometric bands, used effective wavelengths λ_{eff} , calibration zero points ZP and the interstellar extinction A_λ . Furthermore the overview of the magnitudes as used in the SED fitting (see text).

band	λ_{eff} [nm]	ZP [Jy]	A_λ [mag]	m_λ^{min} [mag]	$\langle m_\lambda \rangle$ [mag]	m_λ^{max} [mag]	amplitude [mag]	phase [0,1]	m_λ^{p} [mag]	$m_\lambda^{\text{min},0}$
GALEX FUV	154.9	521	.261					0.38	14.142	13.88
GALEX NUV	230.5	789	.284					0.38	14.440	14.16
Gaia BP	502.1	3393	.112	14.577	14.077	13.576	1.002			14.46
CRTS V	561.8	2690	.0975	14.378	13.897	13.416	0.963			14.28
Gaia G	583.6	2835	.0975	14.374	13.912	13.449	0.925			14.28
PTF R	612.2	3042	.0887	14.387	13.955	13.524	0.864			14.30
Gaia RP	758.9	2485	.0659	13.958	13.534	13.110	0.847			13.89
DENIS I_c	786.2	2442	.0618					0.12	13.474	13.74
	786.2	2442	.0618					0.88	13.443	13.71
DENIS J	1221.	1588	.0293					0.12	13.115	13.21
	1221.	1588	.0293					0.88	13.143	13.24
2MASS J	1235.	1594	.0288					0.78	12.867	13.20
2MASS H	1662.	1024	.0178					0.78	12.518	12.85
DENIS K_s	2147.	667	.0118					0.12	12.809	12.91
	2147.	667	.0118					0.88	12.660	12.77
2MASS K_s	2159.	666	.0117					0.78	12.392	12.72
WISE W1	3353.	310	.0061	12.845	12.523	12.201	0.644			12.84
WISE W2	4603.	172	.0047	12.805	12.444	12.084	0.722			12.80

$$m_{H\alpha} = m_{\text{Gaia } RP} + k_\lambda(BP - RP) + ZP.$$

While the *rms* of the ZP for the stars $m_{\text{Gaia } RP} < 17^{\text{m}}5$ was better than $0^{\text{m}}02$ only minor systematic variations of the order of $0^{\text{m}}08$ were found between the better covered central region and the extreme field corners (Fig. B.1). The color term $k_\lambda = 0^{\text{m}}35 \pm 0^{\text{m}}11$ was derived. To derive a flux calibration of the emission line, the stellar flux f had to be integrated over the response curve I of the 3 nm wide filter.

$$I_* = \int_{\lambda_1}^{\lambda_2} f(\lambda) I(\lambda) d\lambda.$$

As the colors of the field stars show that the sample is dominated by stars later than G5 one can assume that the $H\alpha$ absorption lines do not dominate the flux variation in that region and the stars in a statistical average and we thus can take out the $f(\lambda)$ from the integral in this small wavelength region. The response curve $I(\lambda)$ of the Astrodon filters published by the vendor was integrated numerically giving a value of 2.95 nm. The monochromatic flux in the Vega system was obtained again from the SVO filter service (Rodrigo et al. 2013) from various published 3 nm $H\alpha$ filters from ING, ESO and TNG. They vary by less than 4%. We adopted thus for $m_{H\alpha} = 0^{\text{m}}0$ the mean value of $f(\lambda) = 1.65 \cdot 10^{-9} \text{ erg cm}^{-2} \text{ s}^{-1} \text{ \AA}^{-1}$. Using this calibration we obtain a zero point for the surface brightness of $2.8 \cdot 10^{-17} \text{ erg cm}^{-2} \text{ s}^{-1} \text{ arcsec}^{-1}$ for the mosaic.

Appendix C: Model grid

Figure C.1 shows a fraction of the whole grid of models. The effects of the most critical parameters for the modeling, namely the system inclination i and the fraction of the donor star radius in units of the Roche lobe radius R_{Roche} are demonstrated for the solution fulfilling the best match to the amplitude for this pair of parameters.

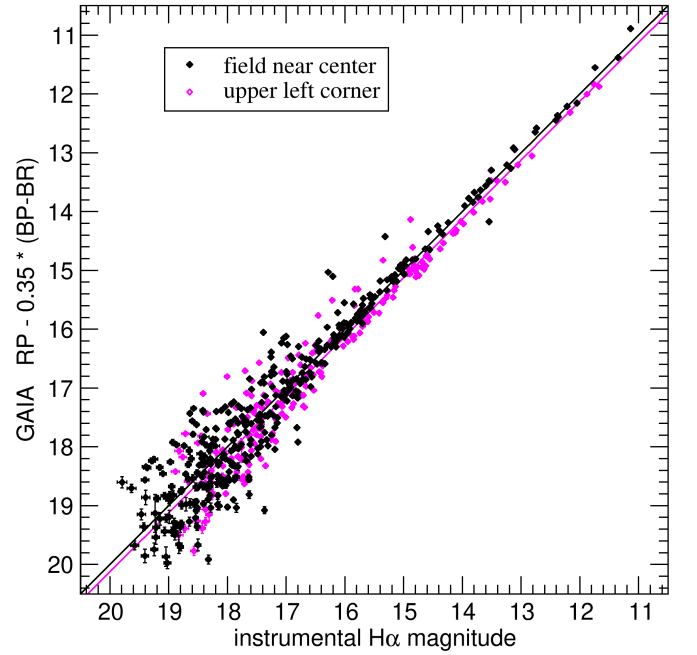


Fig. B.1. The magnitude calibration near the field center (black) and the extreme north east corner (magenta). The Gaia catalog limited the faint end, while the CHILESCOPE $H\alpha$ goes about $1^{\text{m}}5$ deeper.

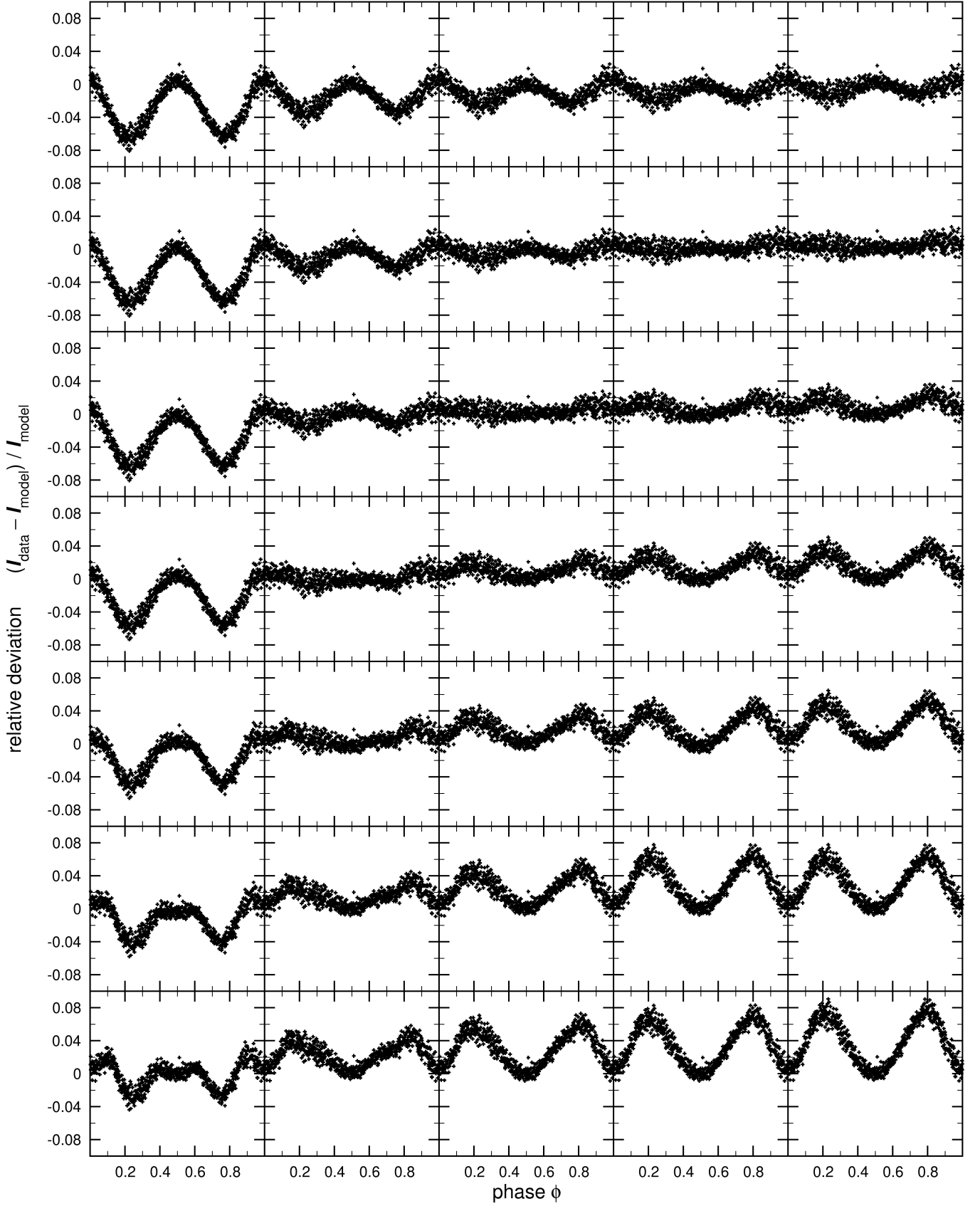


Fig. C.1. A section of the model grid for lowest mass of the grid ($M_{\text{WD}} = 0.4 M_{\odot}$). The deviation of the TESS data intensity I_{data} to the model I_{model} as function of the phase is shown. The columns are for constant radius of the donor star from left to right 1.000, 0.955, 0.910, 0.865, 0.820 times of the Roche lobe radius R_{Roche} . Along the rows the system inclination i varies from 28° to 52° in steps of 4° . The compact companion luminosity was varied each time to fit the system amplitude (see Sect. 3).

Table B.1. Observed Emission Lines in YY Hya at Phase 0.5. The listed line strengths are relative to C III $\lambda 4650 = 100$.

Obs. λ [Å]	Rel. Flux	FWHM [Å]	Line ID	Lab λ [Å]	Obs. λ [Å]	Rel. Flux	FWHM [Å]	Line ID	Lab λ [Å]
3996.4	3	3.5	N II	3995.0	4713.9	9	3.0	He I	4713.2
4010.8	7	3.9	He I	4009.3	4803.9	2	2.9	N II	4803.3
4027.6	41	4.5	He I	4026.2	4862.0	178	7.3	H I	4861.4
4044.1	12	7.1	N II	4041.3, 4043.53	4923.0	26	3.7	C I	4922.7
4071.6	28	4.7	C III	4070.3	4943.5	2	2.8	O II	4943.0
4076.8	24	6.0	C I, C II	4073.3, 4075-76	5001.9	7	2.5	N II	5001.5
4103.1	271	7.7	H I	4101.8	5006.0	10	4.2	N II	5005.2, 5007.3
4121.7	17	4.2	He I	4120.8	5016.5	13	3.1	H I	5115.7
4132.1	8	4.7	N III	4133.8, 4134.9	5048.1	3	2.5	N III	5047.2
4145.1	18	4.6	N I, N II	4143.4, 4145.8	5056.9	5	2.9	Si II	5056.0
4242.1	20	15.7	C I, C III	4223-28, 4247-52	5122.5	2	2.7	C II	5121.8
4268.3	41	3.9	C II	4267.2	5132.5	2	2.7	O I	5131.3
4277.4	5	3.5	O II	4276.6	5146.4	3	3.8	C II	5145.2
4318.9	9	5.0	C II	4317.4	5169.5	2	2.2	N II	5168.1
4341.7	227	7.5	H I	4340.5	5342.9	2	2.7	C III	5341.5
4359.3	15	5.7	O II	4357-59	5412.1	7	2.8	He II	5411.5
4379.9	6	3.3	C III	4379.5	5593.1	10	1.9	N I	5591.8
4389.0	28	4.8	C III	4388.0, 4390.5	5667.1	3	2.4	N II	5666.6
4416.6	22	5.5	O II	4414.9, 4417.0	5679.9	6	3.0	N II	5679.6
4448.8	2	2.8	N II	4447.0	5696.6	3	2.7	C III	5695.9
4472.2	40	5.0	He I	4471.7	5801.8	3	2.9	C I	5800.6
4482.1	13	3.8	Mg II	4481.3	5812.6	2	3.2	O II	5810.2
4514.7	10	11.5	N III	4510.9, 4514.9	5876.2	11	3.4	He I	5875.6
4532.0	2	4.9	N III	4530.9, 4534.6	5929.8	3	6.9	N II	5927.8, 5931.8
4542.5	4	4.1	O III, N III	4540.4, 4544.8	5941.9	2	2.6	N II	5941.7
4553.3	6	5.3	N III, Si III	4551.4, 4553-54	5979.8	2	3.1	Si II	5979.0
4568.8	2	3.1	Si III	4567.8	6151.8	4	3.5	N II	6150.8
4591.9	4	3.2	O II	4591.0	6347.7	6	3.4	N II	6346.9
4610.2	5	4.7	N II, N III	4607.2, 4610.7	6372.0	4	3.3	Si II	6371.4
4634.2	21	7.0	N II	4630.5, 4634.1	6462.3	4	3.7	C III, N III	6460.3, 6463.1
4641.9	35	3.6	N III	4640.6	6483.1	1	6.1	N II, N I	6482.1, 6482-84
4649.9	100	5.8	C III	4647.4, 4650.3	6562.7	65	8.4	H I	6562.85
4662.4	4	3.3	O II	4661.6	6578.8	10	3.5	C II	6578.1
4677.1	4	2.7	C I	4676.7	6583.5	6	3.5	C II	6582.9
4686.5	52	3.4	He II	4685.7	6611.0	2	4.0	N II	6510.6
4700.0	2	2.8	O II	4699.1	6679.1	11	4.2	H I	6678.2
4705.9	3	2.7	O II	4705.3	6783.2	3	7.3	C II	6780.3, 6783.9

Appendix D: Possible Historical Link

Finally, although a bit speculative, we briefly discuss a possible link of YY Hya and its nebula with an apparent “guest star” sighting in Hydra reported in August and September 1065 AD by Korean and Chinese astronomers (Hsi 1957; Ho 1962; Kronk 1999). Although the secondary is not Roche Lobe filling and thus is not feeding accretion yet, fallback from the very slowly ejected CE envelope may cause possibly similar accretion at slower scales on the WD. Taking into account the rotation of the equinox, we find YY Hya to lie at $\alpha = 08^{\text{h}}43^{\text{m}}26^{\text{s}}$, $\delta = -18^{\circ}25'54''$ in 1065 AD. Assuming an observational site in China where the location of YY Hya was visible above the horizon, then YY Hya would be visible about 1.5 hours before sunrise and reached a position about 14° above horizon at the end of the night. It would appear just above the constellation called the celestial temple in the medieval Chinese constellation map by Su Song dated 1092 (Needham 1959). Using this position and constellations as input to Stellarium¹⁸, we find that the YY Hya is near to the constellation Tian Miao (天廟 – also

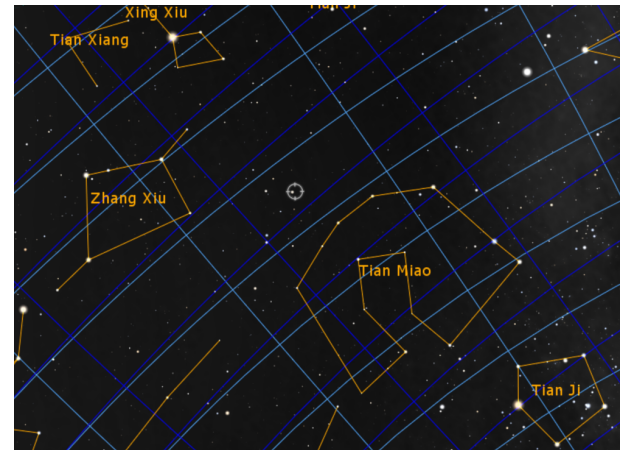


Fig. D.1. The visibility of the region of YY Hya in the morning hours of September, 11th 1065 from Beijing, China using the medieval Chinese constellations. The circle marks the position of YY Hya. The plot was generated by Stellarium 0.19.1

¹⁸ <http://stellarium.org>

called Tiān Miào, Tiānmiào, Thien-miao and T'ien-Miao) containing 14 stars. The precession-corrected position of YY Hya is indicated as well (Fig. D.1). That is what (Hsi 1957) mentions for the vicinity of the 1065 event. Furthermore, it corresponds to the maps in the investigation about ancient comets in Williams (1871) and independently in the framework of the tail of the comet of 1385 in Hind (1845). They appoint this region mostly covered nowadays by Pyxis (or Pixis Nautica).

The position of YY Hya is just on the border to this modern constellation definition¹⁹. Moreover, the crude positional estimate of $\alpha = 10^{\text{h}}20^{\text{m}}$, $\delta = -30^\circ$ in B1950 ($\alpha = 09^{\text{h}}49^{\text{m}}$, $\delta = -25^\circ30'$ in 1065) given by Hsi (1957), which is in fact near to the $m_V = 4^{\text{m}}25$ star α Ant, was too much south and not observable in nighttime from China at that time. We thus have not to further consider this result. In view of these positional agreements, we propose that the link of the 1065 AD transient event with YY Hya is at least possible.

Assuming a typical absolute visual magnitude of a Nova with $M_V \approx -8^{\text{m}}0$, it should have been at $m_V \approx +0^{\text{m}}2$. As there are no stars brighter than $m_V < +4^{\text{m}}0$ in roughly $13^\circ5'$ from the position, and the nearest planet was Saturn at a distance of over 25 degrees away in late August and September 1065 AD, it would seem the 1065 AD guest star may have been fairly noticeable given this nearly empty bright star region of the sky. However, with an angular size of $36'$ ($\equiv 4.8 \text{ pc @ } D_{\text{Gaia}} = 456 \text{ pc}$) and an age of about 1000 years, YY Hya's main nebula would require an average expansion of slightly above 2200 km s^{-1} if it was created in a single event. The outer lobes lying at a distance of 11.5 pc would lead to jets with even higher velocities, around $11\,200 \text{ km s}^{-1}$. Something we do not observe. Also the mass estimate of the shell is by orders of magnitudes too large for a single Nova event. This, excludes that the nebulae around YY Hya was generated during that event about 1000 years ago.

¹⁹ <https://www.iau.org/public/themes/constellations/>